Neuron

Article

Choroid plexus-CSF-targeted antioxidant therapy protects the brain from toxicity of cancer chemotherapy

Graphical abstract

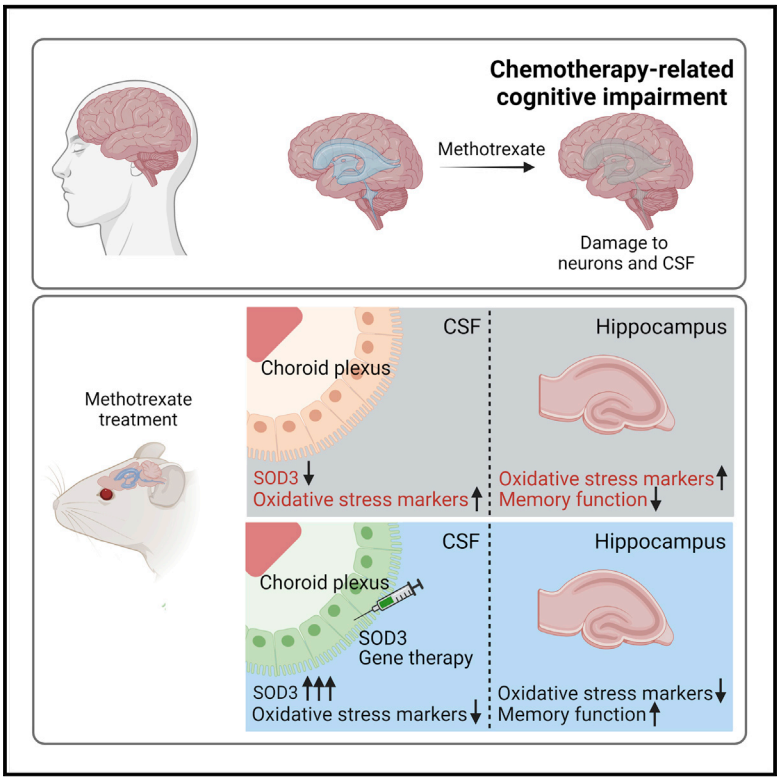

Highlights

- MTX induces oxidative stress in mouse choroid plexus (ChP) and CSF
- MTX damages human neurons and diminishes anti-oxidative capacity of patient CSF
- ChP-targeted SOD3 gene therapy replenishes protective capacity of mouse CSF
- SOD3 gene therapy prevents MTX-induced lipid damage, anxiety, and memory deficits

Authors

Ahram Jang, Boryana Petrova, Taek-Chin Cheong, ..., Eric T. Wong, Naama Kanarek, Maria K. Lehtinen

Correspondence

naama.kanarek@childrens.harvard.edu (N.K.), maria.lehtinen@childrens.harvard.edu (M.K.L.)

In brief

We report that the cancer chemotherapy MTX damages the choroid plexus and cerebrospinal fluid (CSF) by oxidative stress. The impoverished CSF propagates MTX toxicity but can serve as a conduit for therapy. Choroid plexus-targeted antioxidant gene therapy replenishes CSF's protective capacity, preventing metabolic damage in the hippocampus and behavioral deficits.

Jang et al., 2022, Neuron *110*, 1–14
October 19, 2022
https://doi.org/10.1016/j.neuron.2022.08.009

CellPress

Neuron

CellPress

Article

Choroid plexus-CSF-targeted antioxidant therapy protects the brain from toxicity of cancer chemotherapy

Ahram Jang,[1] Boryana Petrova,[1] Taek-Chin Cheong,[1] Miriam E. Zawadzki,[1,2,3] Jill K. Jones,[1,3] Andrew J. Culhane,[1] Frederick B. Shipley,[1,4] Roberto Chiarle,[1,5] Eric T. Wong,[6] Naama Kanarek,[1,2,4,*] and Maria K. Lehtinen[1,2,4,7,*]

[1]Department of Pathology, Boston Children's Hospital, Boston, MA 02115, USA
[2]Graduate Program in Biological and Biomedical Sciences, Harvard Medical School, Boston, MA 02115, USA
[3]Harvard, MIT MD-PhD Program, Harvard Medical School, Boston, MA 02115, USA
[4]Graduate Program in Biophysics, Harvard University, Cambridge, MA 02138, USA
[5]Department of Molecular Biotechnology and Health Sciences, University of Torino, Torino 10126, Italy
[6]Brain Tumor Center & Neuro-Oncology Unit, Beth Israel Deaconess Medical Center, Boston, MA 02115, USA
[7]Lead contact
*Correspondence: naama.kanarek@childrens.harvard.edu (N.K.), maria.lehtinen@childrens.harvard.edu (M.K.L.)
https://doi.org/10.1016/j.neuron.2022.08.009

SUMMARY

For many cancer patients, chemotherapy produces untreatable life-long neurologic effects termed chemotherapy-related cognitive impairment (CRCI). We discovered that the chemotherapy methotrexate (MTX) adversely affects oxidative metabolism of non-cancerous choroid plexus (ChP) cells and the cerebrospinal fluid (CSF). We used a ChP-targeted adeno-associated viral (AAV) vector approach in mice to augment CSF levels of the secreted antioxidant SOD3. AAV-SOD3 gene therapy increased oxidative defense capacity of the CSF and prevented MTX-induced lipid peroxidation in the hippocampus. Furthermore, this gene therapy prevented anxiety and deficits in short-term learning and memory caused by MTX. MTX-induced oxidative damage to cultured human cortical neurons and analyses of CSF samples from MTX-treated lymphoma patients demonstrated that MTX diminishes antioxidant capacity of patient CSF. Collectively, our findings motivate the advancement of ChP- and CSF-targeted anti-oxidative prophylactic measures to relieve CRCI.

INTRODUCTION

The chemotherapeutic and folate analog methotrexate (MTX) is one of the very few effective drug treatments for cancers in the brain (Moe and Holen, 2000; Yu et al., 2021). Unfortunately, neurological side effects are a major limitation of MTX treatment protocols (Gibson and Monje, 2012; Vezmar et al., 2003). Collectively termed chemotherapy-related cognitive impairment (CRCI or chemobrain), signs and symptoms of MTX-induced central nervous system (CNS) toxicity appear in up to 75% of treated cancer patients (Janelsins et al., 2014) and include compromised fine motor abilities (Green et al., 2013), attention capacity (Pierson et al., 2016), acute memory impairment (Bisen-Hersh et al., 2013; Dufourg et al., 2007; Inaba et al., 2008; Rubnitz et al., 1998; Winick et al., 1992), and permanent cognitive deficits (Buizer et al., 2006; Cheung et al., 2016; Ellenberg et al., 2009). As continuous improvements in clinical care decrease mortality, these side effects, which severely degrade quality of life, have become an increasingly relevant treatment-related issue for cancer survivors (Horowitz et al., 2018; Monje et al., 2020).

Mechanisms of MTX toxicity are only beginning to be understood. Recent breakthroughs have uncovered persistent dysregulation of oligodendrocytes, astrocytes, and microglia (Gibson et al., 2019) that culminates in a loss of adaptive myelination (Geraghty et al., 2019). These findings are consistent with volumetric changes in sub-cortical structures (Moore et al., 2016; Zając-Spychała et al., 2017). Other cellular target sites have also been described, including hippocampal neurogenesis (Naewla et al., 2019; Pereira Dias et al., 2014; Seigers et al., 2009; Sekeres et al., 2021; Sritawan et al., 2020; Zając-Spychała et al., 2017). However, the mechanisms underlying CRCI are likely complex as disease course, and therapeutic regimens vary widely. Some side effects may be unavoidable, especially if they arise from the same mechanism of action that targets tumor cells. For MTX, the main anti-cancer mechanism of action is based on the inhibition of nucleic acid synthesis, which leads to death of dividing tumor cells (Wilson et al., 2014) and could affect stem/progenitor cells in the brain. A plausible cause of MTX-induced toxicity is oxidative stress, an insidious process of accumulating redox damage, which has been observed in several non-neural tissues following exposure to MTX (Gunyeli et al.,

Please cite this article in press as: Jang et al., Choroid plexus-CSF-targeted antioxidant therapy protects the brain from toxicity of cancer chemotherapy, Neuron (2022), https://doi.org/10.1016/j.neuron.2022.08.009

2021; Mameri et al., 2021) and reported in MTX-treated leukemia patients (Dewan et al., 2021). Oxidative stress plays a pivotal role in the pathophysiology of many neurologic conditions including those with sequelae similar to CRCI, raising the possibility that oxidative stress could potentially provide a handle for treating CRCI.

The choroid plexus (ChP) and cerebrospinal fluid (CSF) system delivers important health- and growth-promoting factors throughout the brain (Damkier et al., 2013; Fame and Lehtinen, 2020; Lehtinen et al., 2011; Silva-Vargas et al., 2016), thereby providing an attractive therapeutic vehicle for treating CRCI. Indeed, infusion of healthy CSF from young mice can restore hippocampal learning and memory in aging mice (Iram et al., 2022). Collectively, these findings suggest that the ChP-CSF system, with far-reaching and long-lasting effects on the brain throughout life, could be harnessed to counteract the deleterious consequences of MTX leading to neurocognitive sequelae of CRCI.

Here, we report that MTX treatment imparts broad metabolic damage to the ChP-CSF system, including decreased ChP secretion of the antioxidant enzyme extracellular superoxide dismutase 3 (SOD3 or EC-SOD) into the CSF. Because healthy CSF protected neurons from oxidative stress, we hypothesized that augmenting ChP-SOD3 would reduce global neuronal toxicity caused by MTX. Using an adeno-associated viral (AAV) approach, ChP-SOD3 overexpression protected the CSF and neuronal tissue (hippocampus) from MTX-induced oxidative damage and prevented MTX-induced cognitive impairment. SOD3 was also reduced in the CSF of MTX-treated patients, along with increased levels of oxidative imbalance metabolic markers, suggesting that combinatorial treatment strategies with anti-oxidative agents may mitigate MTX-induced toxicity in cancer patients treated with MTX.

RESULTS

To assess the effects of MTX on brain-wide oxidative metabolism, we optimized CSF metabolomics for the detection of oxidative stress-related metabolites (Petrova et al., 2021) by liquid chromatography-mass spectrometry (LC-MS). We profiled the metabolome of CSF samples from MTX- (75 mg/kg i.v.) and vehicle-treated mice. As MTX was detectable in CSF within 30 min (Figure 1A), we performed metabolite profiling of CSF 4, 24, and 48 h post MTX administration. We observed significant metabolic changes with the strongest effect at 24; the 4- and 48-h samples were more similar to the control than to the 24 h time point as represented by the top 15 most changed metabolites (Figure 1B). Partial least-squares discriminant analysis (PLSDA) revealed a separation of the time points on a clear trajectory, with 24 h being the most distant (Figure 1C). A loading plot revealed oxidized and reduced glutathione as major drivers of this change (Figures 1D and S1A). GSH is a highly abundant small molecule that serves as a cellular antioxidant by buffering reactive oxidative molecules through oxidation and conversion to oxidized glutathione (GSSG) (Meister and Anderson, 1983). GSH levels decreased at 24 and 48 h, whereas GSSG increased at 24 h (Figures 1E and 1F), thereby decreasing the GSH/GSSG ratio at both 24 (10-fold) and 48 h (2.5-fold) (Figure 1G). Other metabolites unrelated to redox homeostasis did not show this trend (Figure S1B). Thus, MTX-induced oxidative stress in the CSF was evident by a quantitative alteration in key thiol redox metabolites (Figure 1H).

To test if the oxidative stress signature in CSF could be contributed to by the ChP, we assessed the direct effects of MTX on the ChP. MTX can enter cells through the folate transporters Slc19a1 or Slc46a1 and the folate receptors (Folrs) (Warren et al., 1978), and ChP epithelial cells express high levels of *Slc46a1* and *Folr1* (Dani et al., 2021; Grapp et al., 2013; Wollack et al., 2008). In an *ex vivo* ChP preparation (Figure 2A), MTX was taken up by the ChP (Figures 2B, 2C, S2A, S2B, and S2G) and caused reduction in mitochondrial membrane potential (Figures 2D, 2E, S2C, S2D, and S2H), elevation of reactive oxygen species (ROS) (Figures 2F, 2G, S2E, S2F, and S2I), and decreased oxygen consumption and ATP production (Figures 2H–2J), all indications of impaired oxidative phosphorylation. These data demonstrate that in addition to the known damage of MTX on other areas of the brain, MTX also causes toxicity to the ChP, thereby potentially escalating MTX toxicity in the brain via the CSF.

We next tested the hypothesis that the ChP contributes to an anti-oxidative environment in the CSF by secreting the enzyme SOD3. SOD3 (or EC-SOD) is one of the three members of the SOD family (SOD1, 2, and 3), which catalyze the conversion of superoxide radicals to hydrogen peroxide (Miao and St Clair, 2009). Single-cell gene expression analysis revealed *Sod3* expression predominantly in epithelial and mesenchymal cells at the ChP in each ventricle in the brain (Figures 3A, 3B, S3A, and S3B). These data, as well as comparative expression analyses from the Allen Brain Atlas (Lein et al., 2007), suggest that the ChP is a principal source of SOD3 in the brain. However, we found that exposure of the ChP to MTX resulted in the reduction of *Sod3* expression in the ChP (Figure 3D), which is likely the cause of its depletion (Figures 3E and 3F) and overall diminished activity (Figure 3G) in the CSF following MTX treatment. Taken together, these data suggest that the MTX-induced toxicity in the ChP leads to reduced secretion of SOD3 into the CSF and compromises the anti-oxidative defense that is usually provided by the CSF.

In addition to providing nurturing factors for the brain (Fame and Lehtinen, 2020; Lehtinen et al., 2011), the ChP has the highest activity of the antioxidant enzyme glutathione peroxidase (GPx) in the brain (Saudrais et al., 2018) and can remove exogenous hydroperoxides from the CSF (Saudrais et al., 2018). However, we did not observe decreased ChP expression of *GPx4* or the efflux transporter *Mrp1/Abcc1* (Wijnholds et al., 2000) following acute MTX treatment (data not shown). Oxidative stress in cultured neurons was mitigated by fresh CSF from healthy adult rats (Figure 4A). Therefore, we hypothesized that oxidative stress induced by MTX throughout the brain could be mitigated by boosting ChP expression of anti-oxidants, thereby increasing the availability and activity of anti-oxidative factors in the CSF.

To test this idea, we overexpressed human (h) *SOD3* by transducing embryonic ChP with an adeno-associated virus (AAV) with tropism for ChP epithelial cells (Jang and Lehtinen, 2022; Kaiser et al., 2021; Xu et al., 2021) (Figure 4B). ChP epithelial cells

Please cite this article in press as: Jang et al., Choroid plexus-CSF-targeted antioxidant therapy protects the brain from toxicity of cancer chemotherapy, Neuron (2022), https://doi.org/10.1016/j.neuron.2022.08.009

CellPress

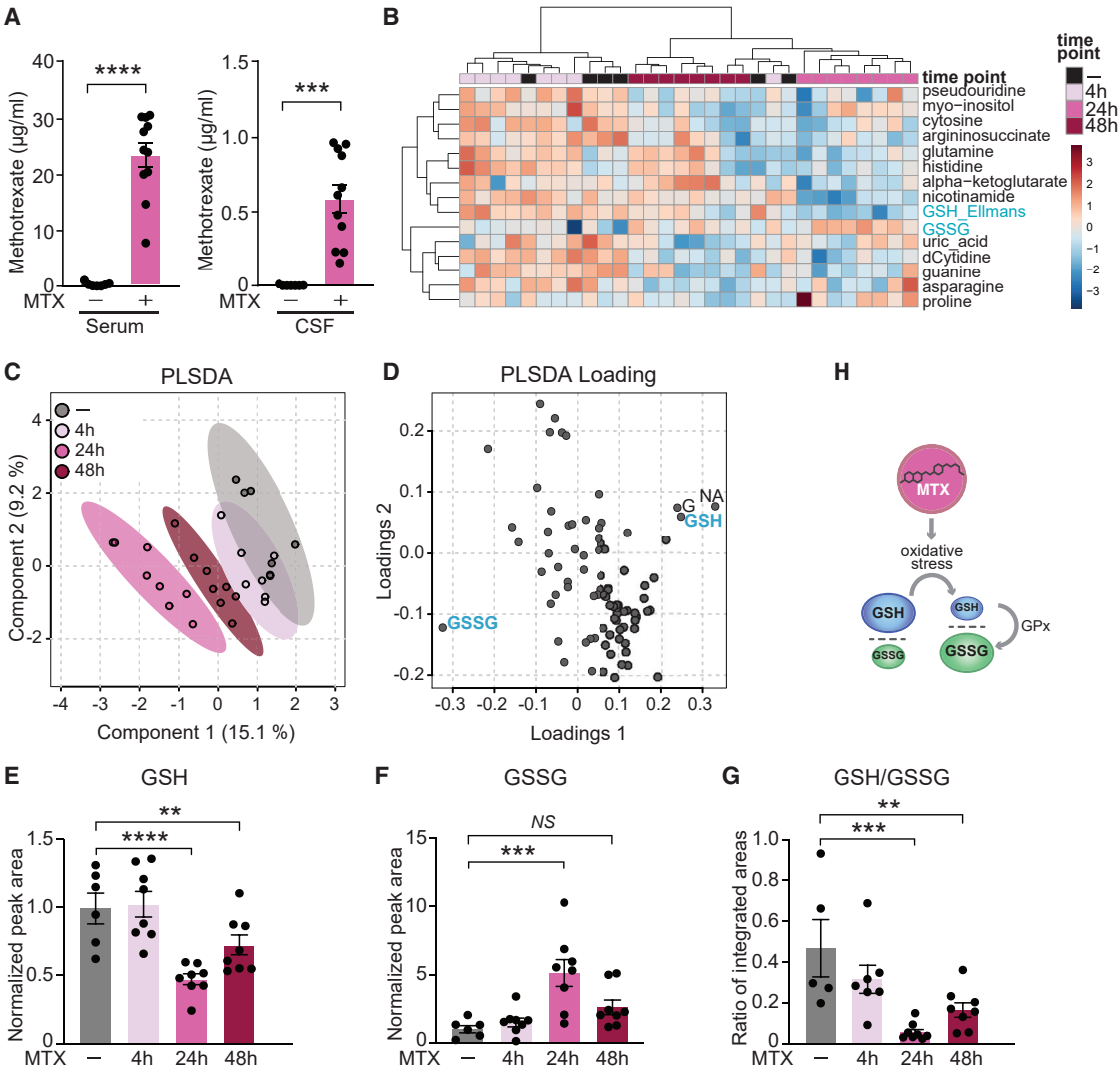

Figure 1. CSF of MTX-treated mice is metabolically altered and reflects markers of oxidative stress

(A) Serum (left) and CSF (right) concentrations of MTX were measured 30 min following a single MTX dose (75 mg/kg i.v.) by ELISA. n = 7 vehicle (saline), n = 11 MTX. ***p < 0.001, ****p < 0.0001. Unpaired t test.

(B) Metabolite profiling of CSF by LC-MS analysis of vehicle- and MTX-treated mice following 4, 24, and 48 h MTX exposure. Top 15 changed metabolites are shown. The heatmap represents log-transformed, Pareto-scaled levels of each of the listed metabolites in the four cohorts (4, 24, and 48 h following MTX treatment, and "ctrl," 48 h post vehicle delivery).

(C) PLSDA analysis of the metabolomics data.

(D) PLSDA loading plot with highlighted metabolites indicating the most influential data points located on the outermost areas along the direction of separation as identified in the corresponding score plot in (C). GSSG, glutathione disulfide; GSH, glutathione (measured as a conjugate of glutathione-Ellmans, see STAR Methods), G, guanine; NA, nicotinic acid. Plots were generated by MetaboAnalyst (Chong et al., 2019).

(E–G) Levels of reduced (GSH, E), oxidized (GSSG, F), and the ratio of reduced to oxidized glutathione (GSH/GSSG, G) in mouse CSF treated with vehicle or MTX for 4, 24, and 48 h. n = 6 vehicle, n = 8 MTX (all time points). **p < 0.01, ***p < 0.001, ****p < 0.0001; NS, not significant. One-way ANOVA test with Benjamini, Krieger, Yukutieli FDR.

(H) Schematic depicting the change in GSH/GSSG ratio as a consequence of oxidative stress. GPx, glutathione peroxidase. Data represent mean ± SEM.

are long-lived cells with limited turnover (Barkho and Monuki, 2015). We verified persistent hSOD3 overexpression in adult ChP (Figures 4C, 4D, and S4A–S4C) and CSF (Figure 4E), which in turn enhanced CSF-SOD enzymatic activity (Figure 4F).

To test the potential protective activity of the supplemental SOD3 levels on the redox state of the CSF of MTX-treated mice, we profiled the CSF of MTX-treated mice by metabolite profiling (Figure 4G). GSH and GSSG were major drivers of the separation between control CSF and CSF from hSOD3-overexpressing mice (Figures 4H and 4I), and the changes in these metabolites indicated a super-physiologic ratio of GSH/GSSG (Figures 4J–4L). Unlike the endogenously regulated expression of SOD3, exogenously expressed hSOD3 was not down-regulated in the ChP of MTX-treated

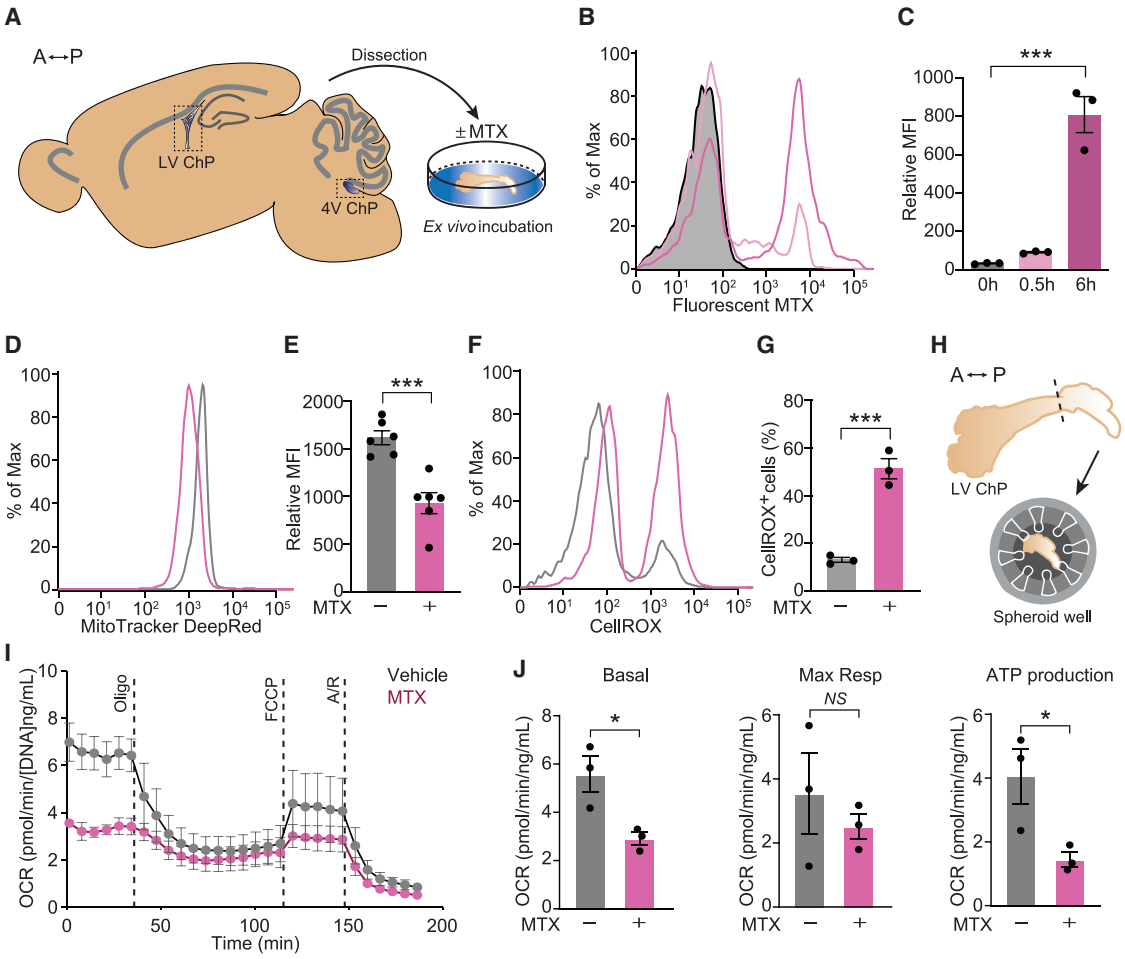

Figure 2. MTX treatment induces oxidative stress in the ChP

(A) A sagittal plane schematic of adult mouse brain depicting the ChP areas dissected for culture and downstream analyses *ex vivo*. Double-headed arrow orients along the anterior (A)-posterior (P) axis.

(B and C) Flow cytometry analysis of cells from mouse lateral ventricle (LV) ChP following incubation with 2 μM fluorescent MTX at the designated time points. A representative histogram (B) and mean fluorescence intensity (MFI) of fluorescent MTX (C) are shown. n = 3 per group. ***$p < 0.001$. One-way ANOVA with Tukey's post hoc test.

(D and E) MitoTracker Deep Red staining of mouse LV ChP following treatment with vehicle or 10 μM MTX for 2 h. Results were analyzed by flow cytometry. A representative histogram (D) and mean fluorescence intensity (MFI) of the MitoTracker signal (E) are shown. n = 6 per group. ***$p < 0.001$. Unpaired t test.

(F and G) ROS were assessed by CellROX staining of mouse LV ChP following incubation with vehicle or 10 μM MTX for 4 h. Results were analyzed by flow cytometry. A representative histogram (F) and the percent CellROX-positive cells (G) are shown. n = 3 per group. ***$p < 0.001$. Unpaired t test.

(H) Schematic depicting assay of mitochondrial function using Agilent Seahorse XFe96 test, anterior (A) and posterior (P) axis.

(I and J) Mouse LV ChP was analyzed by Seahorse following 2 h of vehicle or 10 μM MTX. Cellular oxygen consumption rate (OCR) normalized to total DNA content is shown for vehicle (gray dots) or MTX-treated (pink dots). Representative time course data (I) and aggregate data (J) are shown. n = 3 per group. *$p < 0.05$; NS, not significant. Unpaired t test. Oligo, oligomycin; FCCP, carbonyl cyanide-4-(trifluoromethoxy) phenylhydrazone; A/R, antimycin A plus rotenone; Resp, respiratory. Data represent mean ± SEM.

mice (Figures 4C and S4D), paralleling the effective anti-oxidative capacity of the CSF of hSOD3-overexpressing mice (Figures 4J–4L).

SOD3 is a secreted enzyme and although important in the CSF, it is minimally expressed by neurons. However, we found that the activity of the anti-oxidative enzyme GPx was reduced in neuronal tissue such as the hippocampus following acute MTX treatment (Figures 5A–5C). It was previously reported that reduced GPx enzymatic activity by superoxide occurs following oxidative stress and can further exacerbate the stress (Lubos et al., 2011). Accordingly, lipid peroxidation, a marker of oxidative stress (Del Rio et al., 2005), was increased in the hippocampus of MTX-treated mice (Figures 5A and 5D). These results align with the previous reports of the hippocampus as an established site of chemotherapy-induced damage (Gibson et al., 2019; Yang et al., 2011).

We, therefore, tested whether exogenous expression of hSOD3 can function as gene therapy and protect the hippocampus from MTX-induced oxidative stress. Indeed, hSOD3 overexpression mitigated MTX-induced hippocampal toxicity as

Please cite this article in press as: Jang et al., Choroid plexus-CSF-targeted antioxidant therapy protects the brain from toxicity of cancer chemotherapy, Neuron (2022), https://doi.org/10.1016/j.neuron.2022.08.009

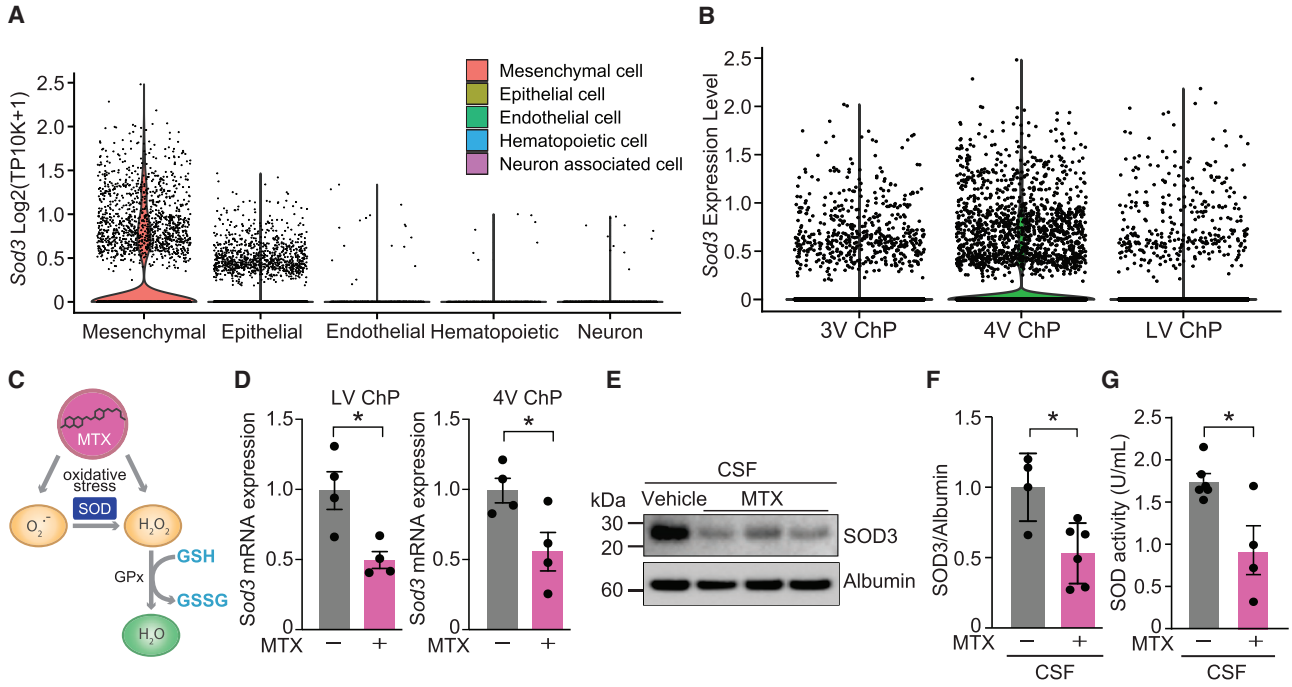

Figure 3. MTX treatment reduces ChP expression and CSF levels of SOD3

(A) Single-cell RNA-seq analysis in developing ChP (Dani et al., 2021) revealed *Sod3* expression predominantly in epithelial and mesenchymal cells.

(B) Regionalized ChP-*Sod3* expression across all ventricles. See also Lun et al. (2015).

(C) Proposed model of MTX-induced oxidative stress and the key role of SOD family proteins as antioxidants following MTX exposure.

(D) *Sod3* expression quantified by qRT-PCR in LV ChP (left) and fourth ventricle (4V) ChP (right) in mice treated with either vehicle or 75 mg/kg MTX for 48 h. n = 4 per group. *p < 0.05. Unpaired t test.

(E) CSF lysates from vehicle or MTX-treated mice were probed with the SOD3 and albumin antibodies.

(F) CSF-SOD3 expression in vehicle or MTX-treated mice as quantified by immunoblotting and normalized to albumin. n = 4 vehicle, n = 6 MTX. *p < 0.05. Unpaired t test.

(G) Relative SOD activity determined by colorimetric assay in rat CSF following treatment with either vehicle or 75 mg/kg MTX for 48 h. n = 6 vehicle, n = 4 MTX. *p < 0.05. Unpaired t test. Data represent mean ± SEM.

observed by lack of reduction in GPx activity. GPx activity was low at the basal state in hSOD3-expressing mice, possibly due to the high antioxidant activity of hSOD3 and lessened need for GPx activity (Figures 5E and 5F). Furthermore, the oxidative stress marker malondialdehyde (MDA) was not elevated by MTX treatment in the hippocampus of mice that overexpressed hSOD3 in their ChP (Figure 5G). Taken together, these data demonstrate that the exogenous expression of the secreted enzyme SOD3 by the ChP can protect the CSF and hippocampus from oxidative damage. These results do not discern whether oxidative neural damage occurs directly, via the ChP-CSF axis, or both. However, importantly, boosting the antioxidative capacity of the CSF mitigated MTX-induced oxidative stress.

Interestingly, we did not observe the usual MTX-induced metabolic indicators of oxidative stress in CSF samples from AAV-GFP-injected mice (Figures 4J–4L), potentially indicating an altered baseline oxidative stress state induced by pre-conditioning the brain with a low level of oxidative stress by the AAV approach (Chan et al., 2021). Indeed, differential statistical analysis of our metabolomics data demonstrated an effect of GFP expression on both CSF of control and MTX-treated mice (Figures S4E and S4F). However, other key metabolites did not change by AAV-GFP transduction (Figure S4G), implying an overall healthy, functional ChP and CSF in AAV-transduced mice.

To determine the possible functional benefits of ChP-SOD3 augmentation in MTX-treated mice, we assessed cognitive behavior in the context of a chronic MTX treatment paradigm (Figure 5H Gibson et al., 2019) that more closely approximates the patient treatment regimen in the clinical setting. We first confirmed in control experiments that AAV-GFP or -SOD3 overexpression did not lead to overt changes in basic mouse laboratory behaviors including grip strength and rotarod performance (Figures S5A and S5B). We then examined the behaviors of AAV-GFP- or SOD3-overexpressing mice treated with MTX or vehicle control. MTX-treated AAV-GFP mice exhibited increased anxiety as evaluated in the elevated plus maze, and this anxiety phenotype was prevented by AAV-SOD3 augmentation (Figures 5I and S5C). MTX-treated AAV-GFP mice also exhibited impaired short-term memory function in the Y-maze hippocampal learning and memory task (Figure 5J), and importantly, this learning and memory deficit was also prevented by AAV-SOD3 augmentation (Figure 5J). Unexpectedly, we did not observe impaired behaviors in open field or novel object recognition tasks following MTX treatment (Figures S5D–S5F) as previously

Please cite this article in press as: Jang et al., Choroid plexus-CSF-targeted antioxidant therapy protects the brain from toxicity of cancer chemotherapy, Neuron (2022), https://doi.org/10.1016/j.neuron.2022.08.009

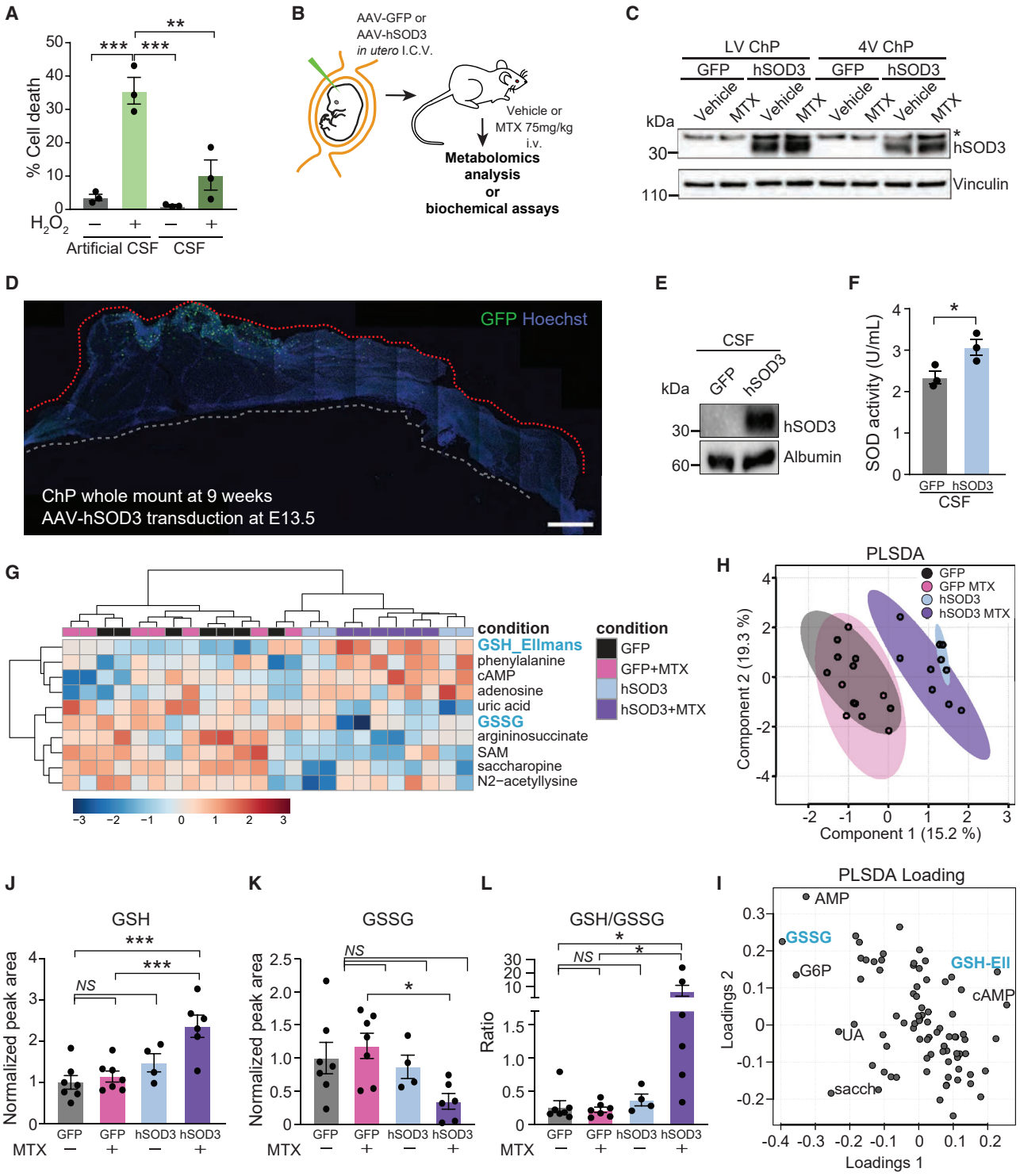

Figure 4. Supplemental ChP-SOD3 expression mitigates MTX-induced oxidative stress in the CSF and the hippocampus

(A) Percent cell death in cerebellar granule neurons cultured in 20% artificial CSF or 20% adult, native CSF in basal medium and treated with vehicle or 100 μM H_2O_2 for 24 h, n = 3 per group. **p < 0.01 ***p < 0.001. One-way ANOVA with Tukey's post hoc test.

(B) Experimental overview for intracerebroventricular (i.c.v.) delivery of AAVs into developing brain ventricles at E13.5. All subsequent experiments were performed postnatally in adult mice.

(C) Lysates of LV ChP and 4V ChP of mice transduced with either AAV-GFP or AAV-hSOD3 and treated with either vehicle or 75 mg/kg MTX for 48 h were probed with the SOD3 and Vinculin antibodies.

(legend continued on next page)

Please cite this article in press as: Jang et al., Choroid plexus-CSF-targeted antioxidant therapy protects the brain from toxicity of cancer chemotherapy, Neuron (2022), https://doi.org/10.1016/j.neuron.2022.08.009

reported (Gibson et al., 2019). All mouse behavior experiments in our present study were performed using CD-1 mice, whereas previous studies have used other strains including C57BL/6 or hybrid mice (Geraghty et al., 2019; Gibson et al., 2019). Indeed, we noted in control experiments that C57BL/6 mice exhibited heightened sensitivity to MTX treatment compared with CD-1 mice. Collectively, these data suggest strain-specific sensitivities to MTX. Genetic background and environment are emerging as key features underlying phenotypes for a growing number of mouse models of neurologic disease (e.g., Burberry et al., 2020; Kim et al., 2017; Nguyen et al., 2020) and could prove to modify the risk of CRCI in the clinical context as well. We did not observe aberrant inflammation or macrophage activation at the ChP following acute or chronic MTX treatment (Figures S5G–S5I), suggesting that MTX-induced oxidative stress in the CNS is not solely attributable to immune cell response. Taken together, our data demonstrate that ChP-based AAV-SOD3 augmentation protects mice from MTX-induced anxiety and short-term memory impairments.

To explore the translational potential of enhancing CSF's anti-oxidative capacity for the treatment of MTX toxicity, we tested whether MTX induces oxidative stress in human cortical neurons generated from induced pluripotent stem cells (iPSCs) (Figure S6A). MTX treatment reduced the transcription of the intracellular antioxidant enzymes *SOD1* and *SOD2* in human neurons (Figure 6A). Importantly, MTX treatment of iPSC neurons elevated ROS levels (Figures 6B and S6B) and impaired mitochondrial function (Figures 6C and 6D), implying a reduced ability of the cells to cope with the deleterious consequences of MTX. These and previous observations demonstrate that MTX treatment induces oxidative stress (Gaman et al., 2016) and reduces SOD-mediated anti-oxidative capacity in human neurons.

These findings prompted us to measure CSF-SOD3 levels in patients treated with MTX to test whether, similar to our findings in mice, human CSF also lacks this key protective antioxidant enzyme. We measured SOD3 levels in CSF samples collected by lumbar puncture from eleven patients with CNS lymphoma, prior to and following high dose MTX treatment (Figures 6E and 6F; Table S1), as well as from twelve lymphoma-free controls (Table S2). SOD3 levels were reduced in 8 of 11 CSF samples during MTX treatment, compared with disease-free controls, which had consistently higher levels of SOD3 with the exception of one patient (N8) (Figures 6E and 6F). PLSDA analysis of the CSF metabolome of lymphoma-free patients, lymphoma patients during active MTX treatment, and lymphoma patients at the time of treatment recess revealed that samples from lymphoma patients during recess in MTX treatment were more similar to the control samples versus patients actively being treated with MTX at the time of CSF collection (Figure 6G). One metabolite driving the separation between these groups was the homocysteine and glutathione precursor cystathionine (Figures 6G and 6H), which reflects the redox state of cells and biofluids (Diwakar and Ravindranath, 2007; McBean, 2017). Indeed, although most metabolites were not significantly different between the three groups, metabolites that reflect oxidative stress and which we were able to detect in the patients' CSF, namely cystine and cystathionine, were elevated in patients treated with MTX (Figure 6H). Of note, both GSH and GSSG were not detected in the human samples, as was somewhat expected due to the inability to analyze fresh human CSF samples and the general low abundance of metabolites in human compared with mouse CSF (Jaeger et al., 2015). Despite these technical challenges, the nucleoside inosine was reduced in the CSF of MTX-treated patients, as expected from the mechanism of action of MTX, which inhibits nucleotide synthesis (Figure 6H; Wilson et al., 2014). Taken together, these results demonstrate MTX reduced SOD expression in human iPSCs, reduced SOD3 availability in the CSF of MTX-treated patients, and elevated metabolic markers of oxidative stress. These data indicate a compromised capability of the CSF to reduce ROS toxicity following MTX treatment in patients.

DISCUSSION

Our study confirms and extends the notion that MTX causes brain damage via widespread oxidative stress and further demonstrates that MTX-induced oxidative stress at the ChP leads to imbalance in redox homeostasis of the CSF. However, our data offer hope because they uncover the ChP-CSF axis as a potential therapeutic target. Our data demonstrate that MTX induces specific patterns of metabolic changes in the ChP and CSF of animal models as well as patients, highlighting the importance of SOD3 as a key antioxidant. Accordingly, ChP-SOD3 augmentation protects the brain from oxidative stress and reduces anxiety and cognitive deficits in MTX-treated mice. Collectively, our findings suggest that toxic oxidative stress can be mitigated even in hard-to-reach areas of the brain by ameliorating the MTX-induced metabolic shift in the ChP-CSF system. This effect could be achieved by ChP-targeted gene therapy and may

(D) Representative tiled image of a LV ChP whole mount revealing location of sustained GFP expression near free margin of larger domain at 9 weeks of age.
(E) CSF lysates of mice transduced with either AAV-GFP or AAV-hSOD3 were probed with the SOD3 and Albumin antibodies. Representative blot shown, n = 3.
(F) Relative SOD activity measured by colorimetric assay in CSF of mice expressing either AAV-GFP or AAV-hSOD3. n = 3 vehicle, n = 3 MTX. *p < 0.05. Unpaired t test.
(G) Metabolite profiling of CSF samples from mice transduced with either AAV-GFP or AAV-hSOD3 and treated with vehicle or MTX. Heatmap of top 10 changed metabolites in the CSF following MTX treatment is shown. The heatmap represents log-transformed, Pareto-scaled levels of each of the listed metabolites in the four conditions.
(H) PLSDA analysis of the metabolomics data.
(I) PLSDA loading depicting the metabolites that dictate the cohort distribution in the PLSDA plot with annotated metabolites indicating the data points that most influenced the separation of samples presented in the PLSDA.
(J–L) Levels of reduced (GSH, J), oxidized (GSSG, K), and the ratio of reduced to oxidized glutathione (L) in CSF from mice overexpressing GFP or hSOD3 and treated with vehicle or MTX for 48 h. All measurements were done by LC-MS. n = 7 GFP + vehicle, n = 7 GFP + MTX, n = 4 SOD3 + vehicle, n = 6 SOD3 + MTX. *p < 0.05, ***p < 0.001; NS, not significant. One-way ANOVA test with Benjamini, Krieger, and Yukutieli FDR. Data represent mean ± SEM.

Please cite this article in press as: Jang et al., Choroid plexus-CSF-targeted antioxidant therapy protects the brain from toxicity of cancer chemotherapy, Neuron (2022), https://doi.org/10.1016/j.neuron.2022.08.009

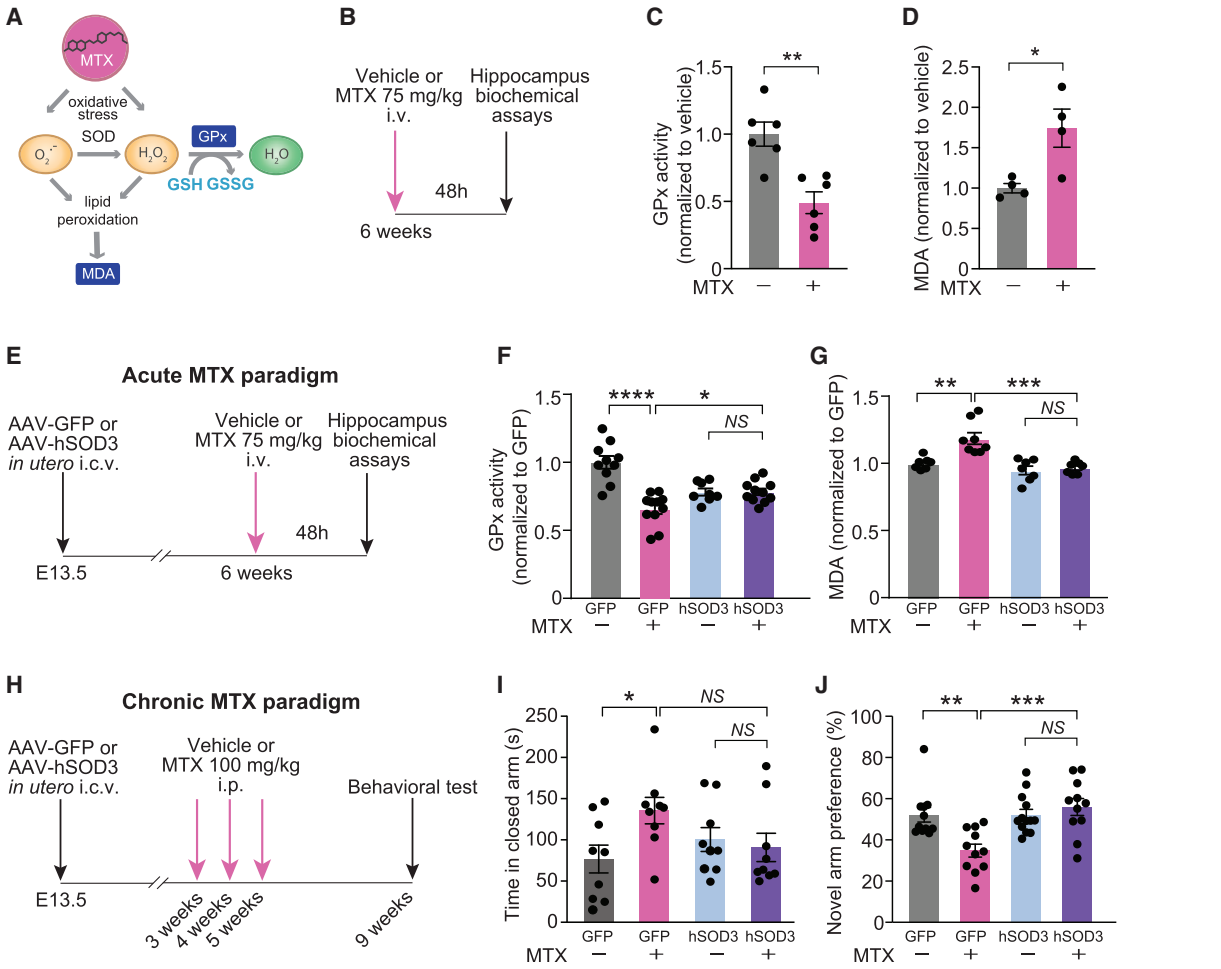

Figure 5. ChP-SOD3 augmentation therapy prevents MTX-induced oxidative stress and cognitive deficits

(A) Proposed model of MTX-induced oxidative stress and downstream redox pathways.

(B) Experimental overview of acute MTX paradigm for hippocampal biochemical assays.

(C) Relative GPx activity was calculated by monitoring NADPH oxidation using cumene hydroperoxide as a substrate in the hippocampus of mice treated with vehicle or 75 mg/kg MTX for 48 h. n = 6 per group. **p < 0.01. Unpaired t test. GPx, glutathione peroxidase.

(D) Lipid peroxidation was assessed by malondialdehyde (MDA) levels obtained by measuring thiobarbituric acid reactive substances (TBARSs) in the hippocampus of mice following i.v. delivery of vehicle or 75 mg/kg MTX for 48 h. n = 4 per group. *p < 0.05. Unpaired t test.

(E) Experimental overview for acute MTX treatment paradigm following prophylactic AAV transduction into developing brain.

(F) Hippocampal GPx activity in MTX-treated mice that prophylactically received AAV-GFP or AAV-hSOD3. n = 10 GFP + vehicle, n = 11 GFP + MTX, n = 8 SOD3 + vehicle, n = 11 SOD3 + MTX. *p < 0.05, ****p < 0.0001. One-way ANOVA with Tukey's post hoc test.

(G) Hippocampal MDA levels reflecting lipid peroxidation in mice treated as (E). n = 7 GFP + vehicle, n = 8 GFP + MTX, n = 7 SOD3 + vehicle, n = 7 SOD3 + MTX. **p < 0.01, ***p < 0.001. One-way ANOVA with Tukey's post hoc test.

(H) Experimental overview for chronic MTX treatment paradigm following prophylactic AAV transduction into the developing brain.

(I) Anxiety behavior was assessed using elevated plus maze as in (H). n = 9 (male = 5, female = 4) GFP + vehicle, n = 9 (male = 5, female = 4) GFP + MTX, n = 9 (male = 4, female = 5) SOD3 + vehicle, n = 9 (male = 4, female = 5) SOD3 + MTX. *p < 0.05; NS, not significant. One-way ANOVA with Bonferroni's post hoc test.

(J) Short-term spatial learning and memory was assessed using Y-maze as in (H). n = 11 (male = 7, female = 4) GFP + vehicle, n = 11 (male = 8, female = 3) GFP + MTX, n = 13 (male = 8, female = 5) SOD3 + vehicle, n = 11 (male = 6, female = 5) SOD3 + MTX. *p < 0.05. One-way with Tukey's post hoc test. Data represent mean ± SEM.

extend to other combinatorial therapies that include antioxidants with MTX administration.

These findings are aligned with an emerging understanding of CSF as a critical fluid niche throughout life. On the one hand, CSF delivers important health- and growth-promoting factors for the developing and adult brain (Chau et al., 2015; Lehtinen et al., 2011; Silva-Vargas et al., 2016), and young CSF can rejuvenate the aging hippocampus by promoting oligodendrocyte progenitor proliferation and differentiation, thereby improving memory consolidation (Iram et al., 2022). On the other hand, the ChP and CSF can be hijacked to propagate disease-promoting conditions including inflammation (Cui et al., 2020) and, as shown here, diminished antioxidant capacity.

Please cite this article in press as: Jang et al., Choroid plexus-CSF-targeted antioxidant therapy protects the brain from toxicity of cancer chemotherapy, Neuron (2022), https://doi.org/10.1016/j.neuron.2022.08.009

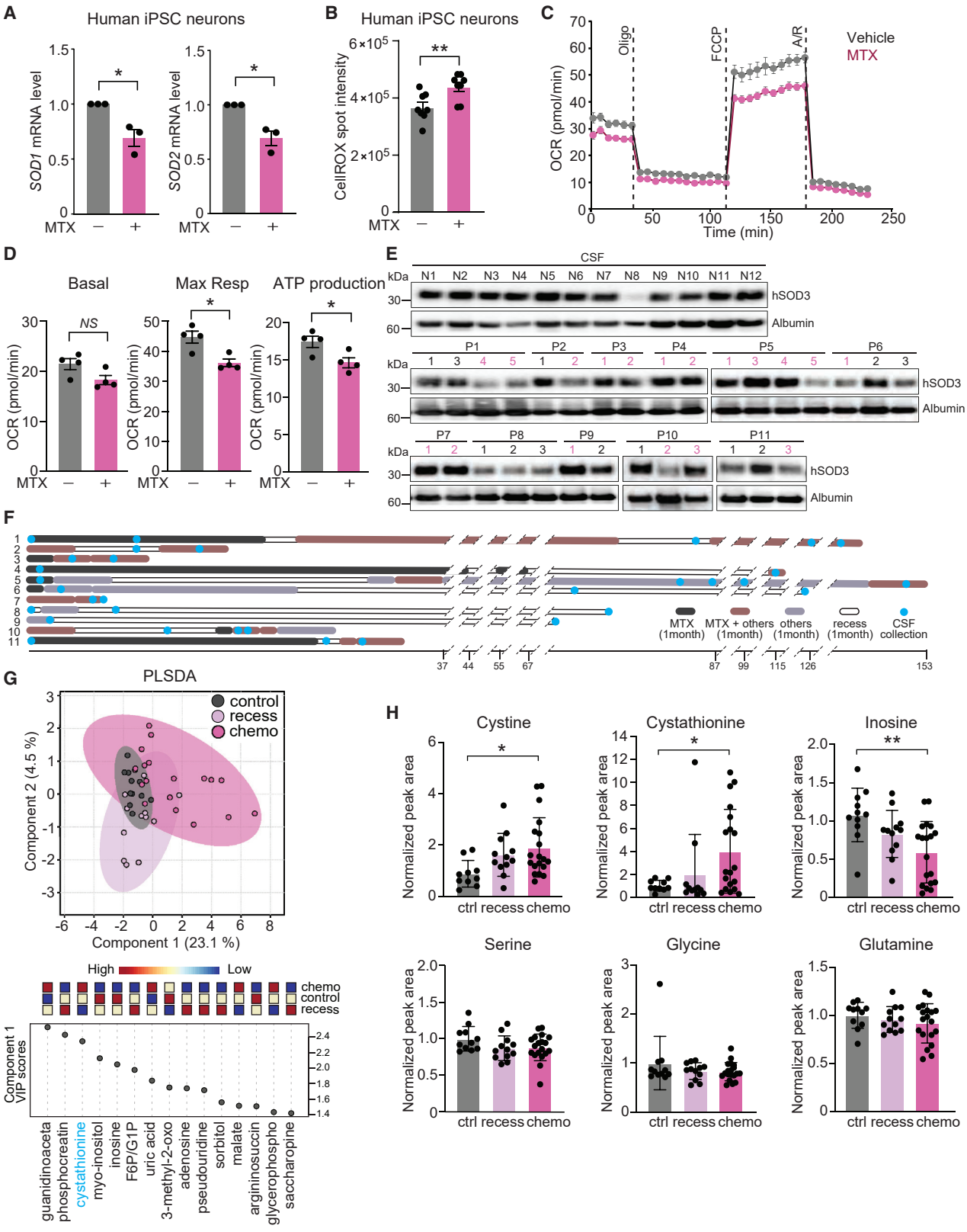

(legend on next page)

Please cite this article in press as: Jang et al., Choroid plexus-CSF-targeted antioxidant therapy protects the brain from toxicity of cancer chemotherapy, Neuron (2022), https://doi.org/10.1016/j.neuron.2022.08.009

Many CSF factors are secreted by the ChP, but factors can also originate from other cells with access to the CSF, including by transcytosis from the blood (Fame and Lehtinen, 2020; Lun et al., 2015). Regardless of the source, elements that find their way into the CSF can reach distant sites throughout the brain. Although the degree to which SOD3 and its downstream metabolites penetrate the brain parenchyma remains to be determined, our data suggest that CSF-borne factors reach the hippocampus in order to have protective effects on cognition.

An important consideration for combinatorial therapy is whether adjunct agents would interfere with clinical efficacy. It is possible that part of the tumor-inhibitory effect of MTX is mediated by its oxidative damage, and that co-administration of an antioxidant together with MTX will diminish this therapeutic capacity of MTX. However, SOD3 has been suggested to enhance the chemotherapeutic effects on tumors in the case of doxorubicin (Mira et al., 2018). Given the well-documented primary mechanism of MTX as an anti-cancer drug through nucleotide synthesis inhibition (Wilson et al., 2014), we propose that MTX-induced oxidative stress is a secondary mechanism that hurts fast-proliferating cells, whereas it is a primary cause for toxicity in post-mitotic cells.

Ultimately, the safety, timing, and duration of ChP-targeted therapies will be important considerations for eventual translatability in the clinical setting. To date, augmentative AAV-based therapeutic approaches have proven remarkably effective for a number of neurologic conditions, with demonstrated long-term safety in human clinical trials (Hudry and Vandenberghe, 2019; Pasi et al., 2020). In the clinical setting, MTX clears rapidly from the CSF (Bratlid and Moe, 1978), and the oxidative markers are transient both in mice and patients. However, our experimental data modeling a chronic MTX treatment paradigm (Gibson et al., 2019) revealed cognitive deficits that were prevented by augmentative ChP-SOD3 expression. These data suggest that although each MTX dose results in acute and short-lasting oxidative damage, this oxidative damage accumulates over time. Repeated treatments can result in long-lasting cognitive deficits, perhaps warranting sustained antioxidant treatment even when chemotherapy is delivered intermittently. More generally, sustained antioxidant delivery via the ChP could favorably impact the course of several other chronic diseases that respond to antioxidant therapy such as age-associated neurologic disease, movement disorders, and some motor neuron diseases.

MTX, similarly to other cancer therapies, involves a range of cytotoxic mechanisms, and the exact mechanism(s) mediating the beneficial effects of CSF-SOD3 gene therapy in a murine model system remain to be fully elucidated. MTX is known to impart damage and dysfunction to oligo-lineage cells, astrocytes, and microglia (Gibson et al., 2019). As a starting point, we found that CSF-SOD3 gene therapy protected the hippocampus from lipid peroxidation in CD-1 mice (Figure 5G). Future studies should elucidate whether CSF-SOD3 gene therapy contributes to myelin plasticity.

The reduction in SOD3 secretion by the MTX-damaged ChP can be mediated by several possible mechanisms, such as the inhibition of folate-dependent oxidative balance in ChP epithelial cells (Fan et al., 2014). Importantly, our data demonstrate that the metabolic status of the ChP-CSF axis both reflects and determines the brain's ability to withstand oxidative stress. Collectively, these findings support the model that the ChP provides a bastion of protection against oxidative stress and is likely to be a key determinant of MTX-induced toxicity.

MTX is most commonly used for the treatment of pediatric acute lymphoblastic leukemia (ALL), in which context it is given intrathecally to prevent and treat CNS involvement of the leukemia. In addition to ALL, MTX is currently incorporated in therapeutic protocols for pediatric osteosarcoma, and adult CNS lymphoma, leukemia, breast, and lung cancer (https://medlineplus.gov/druginfo/). As such, our results may generalize to several tumor types, and co-administration of antioxidants may prove beneficial in other various routes of administration. Because MTX-induced toxicity represents a pressing clinical challenge that influences thousands of children each year (Dufourg et al., 2007; Inaba et al., 2008; Rubnitz et al., 1998; Winick et al., 1992), even moderate improvements in CRCI are anticipated to have enormous clinical impact.

STAR★METHODS

Detailed methods are provided in the online version of this paper and include the following:

- KEY RESOURCES TABLE
- RESOURCE AVAILABILITY
  - Lead contact

Figure 6. MTX treatment renders human neurons susceptible to oxidative stress, and patient CSF reveals reduced SOD availability and altered redox homeostasis during MTX treatment

(A) Expression levels of *SOD1* and *SOD2* measured by qRT-PCR in human iPSC-derived cortical neurons following vehicle or 10 μM MTX treatment for 24 h. n = 3, *p < 0.05. Mann-Whitney.

(B) ROS levels were assessed by CellROX staining using ArrayScan in human iPSC-derived neurons following 72 h of vehicle or 10 μM MTX treatment. n = 8 per group. **p < 0.01. Unpaired t test.

(C and D) Mitochondrial function of vehicle- (gray dots) or MTX-treated (10 μM, pink dots) human iPSC-derived neurons assessed by OCR. Representative time course data (C) and aggregate data (D) are shown. n = 4 per group. *p < 0.05; NS, not significant. Unpaired t test.

(E) Disease-free control CSF lysates (top, labeled "N" for non-lymphoma) and 11 cancer patients (middle and bottom, labeled "P" for patients) were probed with the SOD3 and albumin antibodies. See Tables S1 and S2 for detailed sample information.

(F) Schematic overview of the CSF collection times within the treatment regimen of 11 CNS lymphoma patients. Timeline is plotted on the x axis and number of weeks between events are indicated.

(G) Metabolite profiling of CSF samples from patient groups as in (F). PLSDA loading plot (top) with associated features driving group separation by indicated component (bottom) are shown. Data were log-transformed and Pareto-scaled.

(H) Relative levels of indicated metabolites per patient sample groups. Only significant differences are indicated. *p < 0.05, **p < 0.01. Data represent mean ± SEM.

SUPPLEMENTAL INFORMATION

Supplemental information can be found online at https://doi.org/10.1016/j.neuron.2022.08.009.

ACKNOWLEDGMENTS

We thank the Lehtinen and Kanarek labs for helpful discussions; Nancy Chamberlin for advice on the manuscript; Akiko Terauchi and Hisashi Umemori for advice with hippocampal analyses; Nathaniel Hodgson and the Animal Behavior and Physiology Core for support with mouse behavior studies; Neil Dani, Tais Adelita, and Melody Lun for technical assistance during early stages of study development; the BCH GI core for use of their Seahorse instrument and Ryann Fame for assistance with the Seahorse assays; Naoyuki Taniguchi and Yasuhiko Kizuka for sharing the human SOD3 expression vector; and the BCH Viral Core and the IDDRC Cellular Imaging Core. The graphical abstract was created with BioRender.com. We are grateful for the following support: American Heart Association Pre-doctoral Fellowship Program (M.E.Z.); T32 GM007753 from the National Institute of General Medical Sciences (J.K.J.); The National Research Foundation of Korea (NRF) fellowship and the OFD/BTREC/CTREC Faculty Career Development Fellowship (T.-C.C.); Gabrielle's Angel Foundation for Cancer Research #135 (N.K.), BCH Pilot Grant (N.K.); STARR Cancer Consortium (N.K.); Research and Recruitment Funding by BCH (N.K.); NIH NCI 1R01-CA222598 (R.C.); the Harvard Stem Cell Institute Seed Grant (M.K.L.), NIH NINDS R01 NS088566 (M.K.L.), the New York Stem Cell Foundation (M.K.L.); BCH IDDRC 1U54HD090255; BCH Viral Core P30EY012196; BCH Animal Behavior and Physiology Core P50 HD105351. This research was conducted with support from the Human Neuron Core within the Rosamund Stone Zander Translational Neuroscience Center, BCH, which received support from IDDRC (NIH P50HD105351). The content is solely the responsibility of the authors and does not necessarily represent the official views of the National Institute of General Medical Sciences or the National Institutes of Health. N.K. is a Pew Scholar. M.K.L. is a New York Stem Cell Foundation—Robertson Investigator.

AUTHOR CONTRIBUTIONS

A.J., B.P., N.K., and M.K.L. designed the study. A.J., B.P., A.J.C., M.E.Z., J.K.J., F.B.S., and T.-C.C. performed experiments. A.J. performed the biochemical experiments. B.P., with support from A.J.C., performed MS experiments. M.E.Z. and J.K.J. performed immunostaining and histological analyses. T.-C.C. performed cloning, *ex vivo* FACS and assisted with *in vivo* studies. R.C., N.K., and M.K.L. supervised the study. A.J., B.P., N.K., and M.K.L. wrote the manuscript. A.J., B.P., N.K., and M.K.L. revised the manuscript, and all co-authors approved the final manuscript.

DECLARATION OF INTERESTS

M.K.L. and A.J. are co-inventors on a provisional patent application related to this manuscript.

Received: October 4, 2021
Revised: June 28, 2022
Accepted: August 5, 2022
Published: September 6, 2022

REFERENCES

Barkho, B.Z., and Monuki, E.S. (2015). Proliferation of cultured mouse choroid plexus epithelial cells. PLoS One *10*, e0121738. https://doi.org/10.1371/journal.pone.0121738.

Bisen-Hersh, E.B., Hineline, P.N., and Walker, E.A. (2013). Effects of early chemotherapeutic treatment on learning in adolescent mice: implications for cognitive impairment and remediation in childhood cancer survivors. Clin. Cancer Res. *19*, 3008–3018. https://doi.org/10.1158/1078-0432.CCR-12-3764.

Bratlid, D., and Moe, P.J. (1978). Pharmacokinetics of high-dose methotrexate treatment in children. Eur. J. Clin. Pharmacol. *14*, 143–147. https://doi.org/10.1007/BF00607446.

Breen, C.M., Sykes, D.B., Baehr, C., Fricker, G., and Miller, D.S. (2004). Fluorescein-methotrexate transport in rat choroid plexus analyzed using confocal microscopy. Am. J. Physiol. Ren. Physiol. *287*, F562–F569. https://doi.org/10.1152/ajprenal.00045.2003.

Buizer, A.I., de Sonneville, L.M., van den Heuvel-Eibrink, M.M., and Veerman, A.J. (2006). Behavioral and educational limitations after chemotherapy for childhood acute lymphoblastic leukemia or Wilms tumor. Cancer *106*, 2067–2075. https://doi.org/10.1002/cncr.21820.

Burberry, A., Wells, M.F., Limone, F., Couto, A., Smith, K.S., Keaney, J., Gillet, G., van Gastel, N., Wang, J.Y., Pietilainen, O., et al. (2020). C9orf72 suppresses systemic and neural inflammation induced by gut bacteria. Nature *582*, 89–94. https://doi.org/10.1038/s41586-020-2288-7.

Chan, Y.K., Wang, S.K., Chu, C.J., Copland, D.A., Letizia, A.J., Costa Verdera, H., Chiang, J.J., Sethi, M., Wang, M.K., Neidermyer, W.J., Jr., et al. (2021). Engineering adeno-associated viral vectors to evade innate immune and inflammatory responses. Sci. Transl. Med. *13*. https://doi.org/10.1126/scitranslmed.abd3438.

Chau, K.F., Springel, M.W., Broadbelt, K.G., Park, H.Y., Topal, S., Lun, M.P., Mullan, H., Maynard, T., Steen, H., LaMantia, A.S., and Lehtinen, M.K. (2015). Progressive Differentiation and Instructive Capacities of amniotic Fluid and Cerebrospinal Fluid Proteomes following Neural Tube Closure. Dev. Cell *35*, 789–802. https://doi.org/10.1016/j.devcel.2015.11.015.

Cheung, Y.T., Sabin, N.D., Reddick, W.E., Bhojwani, D., Liu, W., Brinkman, T.M., Glass, J.O., Hwang, S.N., Srivastava, D., Pui, C.H., et al. (2016). Leukoencephalopathy and long-term neurobehavioural, neurocognitive, and brain imaging outcomes in survivors of childhood acute lymphoblastic leukaemia treated with chemotherapy: a longitudinal analysis. Lancet Haematol. *3*, e456–e466. https://doi.org/10.1016/S2352-3026(16)30110-7.

Chong, J., Wishart, D.S., and Xia, J. (2019). Using MetaboAnalyst 4.0 for comprehensive and integrative metabolomics data analysis. Curr. Protoc. Bioinformatics *68*, e86. https://doi.org/10.1002/cpbi.86.

Cui, J., Shipley, F.B., Shannon, M.L., Alturkistani, O., Dani, N., Webb, M.D., Sugden, A.U., Andermann, M.L., and Lehtinen, M.K. (2020). Inflammation of the embryonic choroid Plexus Barrier following maternal immune activation. Dev. Cell *55*, 617–628.e6. https://doi.org/10.1016/j.devcel.2020.09.020.

Damkier, H.H., Brown, P.D., and Praetorius, J. (2013). Cerebrospinal fluid secretion by the choroid plexus. Physiol. Rev. *93*, 1847–1892.

Dani, N., Herbst, R.H., McCabe, C., Green, G.S., Kaiser, K., Head, J.P., Cui, J., Shipley, F.B., Jang, A., Dionne, D., et al. (2021). A cellular and spatial map of the choroid plexus across brain ventricles and ages. Cell *184*, 3056–3074.e21. https://doi.org/10.1016/j.cell.2021.04.003.

Del Rio, D., Stewart, A.J., and Pellegrini, N. (2005). A review of recent studies on malondialdehyde as toxic molecule and biological marker of oxidative stress. Nutr. Metab. Cardiovasc. Dis. *15*, 316–328. https://doi.org/10.1016/j.numecd.2005.05.003.

Dewan, P., Chaudhary, P., Gomber, S., Ahmed, R.S., and Kotru, M. (2021). Oxidative stress in cerebrospinal fluid During treatment in childhood acute lymphoblastic leukemia. Cureus *13*, e15997. https://doi.org/10.7759/cureus.15997.

Diwakar, L., and Ravindranath, V. (2007). Inhibition of cystathionine-gamma-lyase leads to loss of glutathione and aggravation of mitochondrial dysfunction mediated by excitatory amino acid in the CNS. Neurochem. Int. *50*, 418–426. https://doi.org/10.1016/j.neuint.2006.09.014.

Dufourg, M.N., Landman-Parker, J., Auclerc, M.F., Schmitt, C., Perel, Y., Michel, G., Levy, P., Couillault, G., Gandemer, V., Tabone, M.D., et al. (2007). Age and high-dose methotrexate are associated to clinical acute encephalopathy in FRALLE 93 trial for acute lymphoblastic leukemia in children. Leukemia *21*, 238–247. https://doi.org/10.1038/sj.leu.2404495.

Ellenberg, L., Liu, Q., Gioia, G., Yasui, Y., Packer, R.J., Mertens, A., Donaldson, S.S., Stovall, M., Kadan-Lottick, N., Armstrong, G., et al. (2009). Neurocognitive status in long-term survivors of childhood CNS malignancies: a report from the Childhood Cancer Survivor Study. Neuropsychology *23*, 705–717. https://doi.org/10.1037/a0016674.

Fame, R.M., and Lehtinen, M.K. (2020). Emergence and developmental roles of the cerebrospinal fluid system. Dev. Cell *52*, 261–275. https://doi.org/10.1016/j.devcel.2020.01.027.

Fan, J., Ye, J., Kamphorst, J.J., Shlomi, T., Thompson, C.B., and Rabinowitz, J.D. (2014). Quantitative flux analysis reveals folate-dependent NADPH production. Nature *510*, 298–302. https://doi.org/10.1038/nature13236.

Gaman, A.M., Uzoni, A., Popa-Wagner, A., Andrei, A., and Petcu, E.B. (2016). The role of oxidative stress in etiopathogenesis of chemotherapy induced cognitive impairment (CICI)-"chemobrain". Aging Dis *7*, 307–317. https://doi.org/10.14336/AD.2015.1022.

Geraghty, A.C., Gibson, E.M., Ghanem, R.A., Greene, J.J., Ocampo, A., Goldstein, A.K., Ni, L., Yang, T., Marton, R.M., Paşca, S.P., et al. (2019). Loss of adaptive myelination contributes to methotrexate chemotherapy-related cognitive impairment. Neuron *103*, 250–265.e8. https://doi.org/10.1016/j.neuron.2019.04.032.

Gibson, E., and Monje, M. (2012). Effect of cancer therapy on neural stem cells: implications for cognitive function. Curr. Opin. Oncol. *24*, 672–678. https://doi.org/10.1097/CCO.0b013e3283571a8e.

Gibson, E.M., Nagaraja, S., Ocampo, A., Tam, L.T., Wood, L.S., Pallegar, P.N., Greene, J.J., Geraghty, A.C., Goldstein, A.K., Ni, L., et al. (2019). Methotrexate chemotherapy induces persistent tri-glial dysregulation that underlies chemotherapy-related cognitive impairment. Cell *176*, 43–55.e13. https://doi.org/10.1016/j.cell.2018.10.049.

Grapp, M., Wrede, A., Schweizer, M., Hüwel, S., Galla, H.J., Snaidero, N., Simons, M., Bückers, J., Low, P.S., Urlaub, H., et al. (2013). Choroid plexus transcytosis and exosome shuttling deliver folate into brain parenchyma. Nat. Commun. *4*, 2123. https://doi.org/10.1038/ncomms3123.

Green, J.L., Knight, S.J., McCarthy, M., and De Luca, C.R. (2013). Motor functioning during and following treatment with chemotherapy for pediatric acute lymphoblastic leukemia. Pediatr. Blood Cancer *60*, 1261–1266. https://doi.org/10.1002/pbc.24537.

Grieger, J.C., Choi, V.W., and Samulski, R.J. (2006). Production and characterization of adeno-associated viral vectors. Nat. Protoc. *1*, 1412–1428. https://doi.org/10.1038/nprot.2006.207.

Gunyeli, I., Saygin, M., and Ozmen, O. (2021). Methotrexate-induced toxic effects and the ameliorating effects of astaxanthin on genitourinary tissues in a female rat model. Arch. Gynecol. Obstet. *304*, 985–997. https://doi.org/10.1007/s00404-021-06000-2.

Horowitz, T.S., Suls, J., and Treviño, M. (2018). A call for a neuroscience approach to cancer-related cognitive impairment. Trends Neurosci. *41*, 493–496. https://doi.org/10.1016/j.tins.2018.05.001.

Hudry, E., and Vandenberghe, L.H. (2019). Therapeutic AAV gene transfer to the nervous system: a clinical reality. Neuron *101*, 839–862. https://doi.org/10.1016/j.neuron.2019.02.017.

Inaba, H., Khan, R.B., Laningham, F.H., Crews, K.R., Pui, C.H., and Daw, N.C. (2008). Clinical and radiological characteristics of methotrexate-induced acute encephalopathy in pediatric patients with cancer. Ann. Oncol. *19*, 178–184. https://doi.org/10.1093/annonc/mdm466.

Iram, T., Kern, F., Kaur, A., Myneni, S., Morningstar, A.R., Shin, H., Garcia, M.A., Yerra, L., Palovics, R., Yang, A.C., et al. (2022). Young CSF restores oligodendrogenesis and memory in aged mice via Fgf17. Nature *605*, 509–515. https://doi.org/10.1038/s41586-022-04722-0.

Jaeger, C., Glaab, E., Michelucci, A., Binz, T.M., Koeglsberger, S., Garcia, P., Trezzi, J.P., Ghelfi, J., Balling, R., and Buttini, M. (2015). The mouse brain metabolome: region-specific signatures and response to excitotoxic neuronal injury. Am. J. Pathol. *185*, 1699–1712. https://doi.org/10.1016/j.ajpath.2015.02.016.

Janelsins, M.C., Kesler, S.R., Ahles, T.A., and Morrow, G.R. (2014). Prevalence, mechanisms, and management of cancer-related cognitive impairment. Int. Rev. Psychiatry *26*, 102–113. https://doi.org/10.3109/09540261.2013.864260.

Jang, A., and Lehtinen, M.K. (2022). Experimental approaches for manipulating choroid plexus epithelial cells. Fluids Barriers CNS *19*, 36. https://doi.org/10.1186/s12987-022-00330-2.

Kaiser, K., Jang, A., Kompanikova, P., Lun, M.P., Prochazka, J., Machon, O., Dani, N., Prochazkova, M., Laurent, B., Gyllborg, D., et al. (2021). MEIS-WNT5A axis regulates development of fourth ventricle choroid plexus. Development *148*, dev192054. https://doi.org/10.1242/dev.192054.

Kim, S., Kim, H., Yim, Y.S., Ha, S., Atarashi, K., Tan, T.G., Longman, R.S., Honda, K., Littman, D.R., Choi, G.B., and Huh, J.R. (2017). Maternal gut bacteria promote neurodevelopmental abnormalities in mouse offspring. Nature *549*, 528–532. https://doi.org/10.1038/nature23910.

Kobak, D., and Berens, P. (2019). The art of using t-SNE for single-cell transcriptomics. Nat. Commun. *10*, 5416. https://doi.org/10.1038/s41467-019-13056-x.

Lehtinen, M.K., Yuan, Z., Boag, P.R., Yang, Y., Villén, J., Becker, E.B., DiBacco, S., de la Iglesia, N., Gygi, S., Blackwell, T.K., and Bonni, A. (2006). A conserved MST-FOXO signaling pathway mediates oxidative-stress responses and extends life span. Cell *125*, 987–1001.

Lehtinen, M.K., Zappaterra, M.W., Chen, X., Yang, Y.J., Hill, A.D., Lun, M., Maynard, T., Gonzalez, D., Kim, S., Ye, P., et al. (2011). The cerebrospinal fluid provides a proliferative niche for neural progenitor cells. Neuron *69*, 893–905. https://doi.org/10.1016/j.neuron.2011.01.023.

Lein, E.S., Hawrylycz, M.J., Ao, N., Ayres, M., Bensinger, A., Bernard, A., Boe, A.F., Boguski, M.S., Brockway, K.S., Byrnes, E.J., et al. (2007). Genome-wide atlas of gene expression in the adult mouse brain. Nature *445*, 168–176. https://doi.org/10.1038/nature05453.

Lubos, E., Loscalzo, J., and Handy, D.E. (2011). Glutathione peroxidase-1 in health and disease: from molecular mechanisms to therapeutic opportunities. Antioxid. Redox Signal. *15*, 1957–1997. https://doi.org/10.1089/ars.2010.3586.

Lun, M.P., Monuki, E.S., and Lehtinen, M.K. (2015). Development and functions of the choroid plexus–cerebrospinal fluid system. Nat. Rev. Neurosci. *16*, 445–457.

Mameri, A., Bournine, L., Mouni, L., Bensalem, S., and Iguer-Ouada, M. (2021). Oxidative stress as an underlying mechanism of anticancer drugs cytotoxicity

on human red blood cells' membrane. Toxicol. In Vitro *72*, 105106. https://doi.org/10.1016/j.tiv.2021.105106.

McBean, G.J. (2017). Cysteine, glutathione, and thiol redox balance in astrocytes. Antioxidants (Basel) *6*, 62. https://doi.org/10.3390/antiox6030062.

Meister, A., and Anderson, M.E. (1983). Glutathione. Annu. Rev. Biochem. *52*, 711–760. https://doi.org/10.1146/annurev.bi.52.070183.003431.

Miao, L., and St Clair, D.K. (2009). Regulation of superoxide dismutase genes: implications in disease. Free Radic. Biol. Med. *47*, 344–356. https://doi.org/10.1016/j.freeradbiomed.2009.05.018.

Mira, E., Carmona-Rodríguez, L., Pérez-Villamil, B., Casas, J., Fernández-Aceñero, M.J., Martínez-Rey, D., Martín-González, P., Heras-Murillo, I., Paz-Cabezas, M., Tardáguila, M., et al. (2018). SOD3 improves the tumor response to chemotherapy by stabilizing endothelial HIF-2alpha. Nat. Commun. *9*, 575. https://doi.org/10.1038/s41467-018-03079-1.

Moe, P.J., and Holen, A. (2000). High-dose methotrexate in childhood all. Pediatr. Hematol. Oncol. *17*, 615–622. https://doi.org/10.1080/08880010050211321.

Monje, M., Borniger, J.C., D'Silva, N.J., Deneen, B., Dirks, P.B., Fattahi, F., Frenette, P.S., Garzia, L., Gutmann, D.H., Hanahan, D., et al. (2020). Roadmap for the emerging field of cancer neuroscience. Cell *181*, 219–222. https://doi.org/10.1016/j.cell.2020.03.034.

Montoro, D.T., Haber, A.L., Biton, M., Vinarsky, V., Lin, B., Birket, S.E., Yuan, F., Chen, S., Leung, H.M., Villoria, J., et al. (2018). A revised airway epithelial hierarchy includes CFTR-expressing ionocytes. Nature *560*, 319–324. https://doi.org/10.1038/s41586-018-0393-7.

Moore, I.M., Merkle, C.J., Byrne, H., Ross, A., Hawkins, A.M., Ameli, S.S., and Montgomery, D.W. (2016). Effects of intraventricular methotrexate on neuronal injury and gene expression in a rat model: findings From an exploratory study. Biol. Res. Nurs. *18*, 505–514. https://doi.org/10.1177/1099800416644780.

Naewla, S., Sirichoat, A., Pannangrong, W., Chaisawang, P., Wigmore, P., and Welbat, J.U. (2019). Hesperidin alleviates methotrexate-induced memory deficits via hippocampal neurogenesis in adult rats. Nutrients *11*, 936. https://doi.org/10.3390/nu11040936.

Nguyen, L., Laboissonniere, L.A., Guo, S., Pilotto, F., Scheidegger, O., Oestmann, A., Hammond, J.W., Li, H., Hyysalo, A., Peltola, R., et al. (2020). Survival and motor phenotypes in FVB C9-500 ALS/FTD BAC transgenic mice reproduced by multiple labs. Neuron *108*, 784–796.e3. https://doi.org/10.1016/j.neuron.2020.09.009.

Ota, F., Kizuka, Y., Kitazume, S., Adachi, T., and Taniguchi, N. (2016). N-Glycosylation is essential for the secretion of extracellular superoxide dismutase. FEBS Lett. *590*, 3357–3367. https://doi.org/10.1002/1873-3468.12378.

Pasi, K.J., Rangarajan, S., Mitchell, N., Lester, W., Symington, E., Madan, B., Laffan, M., Russell, C.B., Li, M., Pierce, G.F., and Wong, W.Y. (2020). Multiyear follow-up of AAV5-hFVIII-SQ gene therapy for hemophilia A. N. Engl. J. Med. *382*, 29–40. https://doi.org/10.1056/NEJMoa1908490.

Pereira Dias, G., Hollywood, R., Bevilaqua, M.C., da Luz, A.C., Hindges, R., Nardi, A.E., and Thuret, S. (2014). Consequences of cancer treatments on adult hippocampal neurogenesis: implications for cognitive function and depressive symptoms. Neuro. Oncol *16*, 476–492. https://doi.org/10.1093/neuonc/not321.

Petrova, B., Warren, A., Vital, N.Y., Culhane, A.J., Maynard, A.G., Wong, A., and Kanarek, N. (2021). Redox metabolism measurement in mammalian cells and tissues by LC-MS. Metabolites *11*, 313. https://doi.org/10.3390/metabo11050313.

Pierson, C., Waite, E., and Pyykkonen, B. (2016). A meta-analysis of the neuropsychological effects of chemotherapy in the treatment of childhood cancer. Pediatr. Blood Cancer *63*, 1998–2003. https://doi.org/10.1002/pbc.26117.

Rubnitz, J.E., Relling, M.V., Harrison, P.L., Sandlund, J.T., Ribeiro, R.C., Rivera, G.K., Thompson, S.J., Evans, W.E., and Pui, C.H. (1998). Transient encephalopathy following high-dose methotrexate treatment in childhood acute lymphoblastic leukemia. Leukemia *12*, 1176–1181. https://doi.org/10.1038/sj.leu.2401098.

Saudrais, E., Strazielle, N., and Ghersi-Egea, J.F. (2018). Choroid plexus glutathione peroxidases are instrumental in protecting the brain fluid environment from hydroperoxides during postnatal development. Am. J. Physiol. Cell Physiol. *315*, C445–C456. https://doi.org/10.1152/ajpcell.00094.2018.

Seigers, R., Schagen, S.B., Beerling, W., Boogerd, W., van Tellingen, O., van Dam, F.S., Koolhaas, J.M., and Buwalda, B. (2008). Long-lasting suppression of hippocampal cell proliferation and impaired cognitive performance by methotrexate in the rat. Behav. Brain Res. *186*, 168–175. https://doi.org/10.1016/j.bbr.2007.08.004.

Seigers, R., Schagen, S.B., Coppens, C.M., van der Most, P.J., van Dam, F.S., Koolhaas, J.M., and Buwalda, B. (2009). Methotrexate decreases hippocampal cell proliferation and induces memory deficits in rats. Behav. Brain Res. *201*, 279–284. https://doi.org/10.1016/j.bbr.2009.02.025.

Sekeres, M.J., Bradley-Garcia, M., Martinez-Canabal, A., and Winocur, G. (2021). Chemotherapy-induced cognitive impairment and hippocampal neurogenesis: a review of physiological mechanisms and interventions. Int. J. Mol. Sci. *22*, 12697. https://doi.org/10.3390/ijms222312697.

Silva-Vargas, V., Maldonado-Soto, A.R., Mizrak, D., Codega, P., and Doetsch, F. (2016). Age-dependent niche signals from the choroid plexus regulate adult neural stem cells. Cell Stem Cell *19*, 643–652. https://doi.org/10.1016/j.stem.2016.06.013.

Sritawan, N., Prajit, R., Chaisawang, P., Sirichoat, A., Pannangrong, W., Wigmore, P., and Welbat, J.U. (2020). Metformin alleviates memory and hippocampal neurogenesis decline induced by methotrexate chemotherapy in a rat model. Biomed. Pharmacother. *131*, 110651. https://doi.org/10.1016/j.biopha.2020.110651.

Vezmar, S., Becker, A., Bode, U., and Jaehde, U. (2003). Biochemical and clinical aspects of methotrexate neurotoxicity. Chemotherapy *49*, 92–104. https://doi.org/10.1159/000069773.

Warren, R.D., Nichols, A.P., and Bender, R.A. (1978). Membrane transport of methotrexate in human lymphoblastoid cells. Cancer Res. *38*, 668–671.

Wijnholds, J., deLange, E.C., Scheffer, G.L., van den Berg, D.J., Mol, C.A., van der Valk, M., Schinkel, A.H., Scheper, R.J., Breimer, D.D., and Borst, P. (2000). Multidrug resistance protein 1 protects the choroid plexus epithelium and contributes to the blood-cerebrospinal fluid barrier. J. Clin. Invest. *105*, 279–285. https://doi.org/10.1172/JCI8267.

Wilson, P.M., Danenberg, P.V., Johnston, P.G., Lenz, H.J., and Ladner, R.D. (2014). Standing the test of time: targeting thymidylate biosynthesis in cancer therapy. Nat. Rev. Clin. Oncol. *11*, 282–298. https://doi.org/10.1038/nrclinonc.2014.51.

Winden, K.D., Sundberg, M., Yang, C., Wafa, S.M.A., Dwyer, S., Chen, P.F., Buttermore, E.D., and Sahin, M. (2019). Biallelic mutations in TSC2 lead to abnormalities associated with cortical tubers in human iPSC-derived neurons. J. Neurosci. *39*, 9294–9305. https://doi.org/10.1523/JNEUROSCI.0642-19.2019.

Winick, N.J., Bowman, W.P., Kamen, B.A., Roach, E.S., Rollins, N., Jacaruso, D., and Buchanan, G.R. (1992). Unexpected acute neurologic toxicity in the treatment of children with acute lymphoblastic leukemia. J. Natl. Cancer Inst. *84*, 252–256. https://doi.org/10.1093/jnci/84.4.252.

Wollack, J.B., Makori, B., Ahlawat, S., Koneru, R., Picinich, S.C., Smith, A., Goldman, I.D., Qiu, A., Cole, P.D., Glod, J., and Kamen, B. (2008). Characterization of folate uptake by choroid plexus epithelial cells in a rat primary culture model. J. Neurochem. *104*, 1494–1503. https://doi.org/10.1111/j.1471-4159.2007.05095.x.

Xia, J., Sinelnikov, I.V., Han, B., and Wishart, D.S. (2015). MetaboAnalyst 3.0–making metabolomics more meaningful. Nucleic Acids Res. *43*, W251–W257. https://doi.org/10.1093/nar/gkv380.

Xu, H., Fame, R.M., Sadegh, C., Sutin, J., Naranjo, C., Della Syau, Cui, J., Shipley, F.B., Vernon, A., Gao, F., et al. (2021). Choroid plexus NKCC1 mediates cerebrospinal fluid clearance during mouse early postnatal development. Nat. Commun. *12*, 447. https://doi.org/10.1038/s41467-020-20666-3.

Yang, M., Kim, J.S., Kim, J., Kim, S.H., Kim, J.C., Kim, J., Wang, H., Shin, T., and Moon, C. (2011). Neurotoxicity of methotrexate to hippocampal cells in vivo and in vitro. Biochem. Pharmacol. *82*, 72–80. https://doi.org/10.1016/j.bcp.2011.03.020.

Yu, J., Du, H., Ye, X., Zhang, L., and Xiao, H. (2021). High-dose methotrexate-based regimens and post-remission consolidation for treatment of newly diagnosed primary CNS lymphoma: meta-analysis of clinical trials. Sci. Rep. *11*, 2125. https://doi.org/10.1038/s41598-020-80724-0.

Zając-Spychała, O., Pawlak, M.A., Karmelita-Katulska, K., Pilarczyk, J., Derwich, K., and Wachowiak, J. (2017). Long-term brain structural magnetic resonance imaging and cognitive functioning in children treated for acute lymphoblastic leukemia with high-dose methotrexate chemotherapy alone or combined with CNS radiotherapy at reduced total dose to 12 Gy. Neuroradiology *59*, 147–156. https://doi.org/10.1007/s00234-016-1777-8.

Zhang, Y., Pak, C., Han, Y., Ahlenius, H., Zhang, Z., Chanda, S., Marro, S., Patzke, C., Acuna, C., Covy, J., et al. (2013). Rapid single-step induction of functional neurons from human pluripotent stem cells. Neuron *78*, 785–798. https://doi.org/10.1016/j.neuron.2013.05.029.

Please cite this article in press as: Jang et al., Choroid plexus-CSF-targeted antioxidant therapy protects the brain from toxicity of cancer chemotherapy, Neuron (2022), https://doi.org/10.1016/j.neuron.2022.08.009

STAR★METHODS

KEY RESOURCES TABLE

REAGENT or RESOURCE	SOURCE	IDENTIFIER
Antibodies		
Rabbit polyclonal anti-Albumin	Cell Signaling Technology	Cat# 4929; RRID: AB_2225785
Rat monoclonal anti-CD68	Abcam	Cat# ab53444; RRID: AB_869007
Chicken polyclonal anti-GFP	Abcam	Cat# ab13970; RRID: AB_300798
Mouse monoclonal anti-Superoxide dismutase 3	Abcam	Cat# ab80946; RRID: AB_1641091
Rabbit monoclonal anti-Superoxide dismutase 3	Abcam	Cat# ab171738
Rabbit monoclonal anti-Vinculin	Cell Signaling Technology	Cat# 13901; RRID: AB_2728768
Anti-rabbit IgG, HRP-linked antibody	Cell Signaling Technology	Cat# 7074; RRID: AB_2099233
Anti-mouse IgG, HRP-linked antibody	Cell Signaling Technology	Cat#7076; RRID: AB_330924
Hoechst 33342, Trihydrochloride, Trihydrate	Thermo Fisher Scientific	Cat# H3570
Bacterial and virus strains		
AAV2/5-CMV-hrGFP-hGH	Boston Children's Hospital viral core, IDDRC	N/A
AAV2/5-CMV-hSOD3-hrGFP-hGH	Boston Children's Hospital viral core, IDDRC	N/A
Biological samples		
Human CSF	Tables S1 and S2	N/A
Chemicals, peptides, and recombinant proteins		
Methotrexate disodium salt	Fisher Scientific	Cat# AAJ66364MD
Methotrexate hydrate	Sigma-Aldrich	Cat# M8407; CAS: 133073-73-1
Methotrexate, fluorescein, triammonium salt	Thermo Fisher Scientific	Cat# M1198MP
7-amino-actinomycin D (7AAD)	Biolegend	Cat# 420404
MitoTracker deep red FM	Thermo Fisher Scientific	Cat# M22426
CellROX deep red	Thermo Fisher Scientific	Cat# C10422
Neurobasal medium, minus phenol red	GIBCO	Cat# 12348017
Neurobasal-A	Life Technologies	Cat# 10888-022
Basal Medium Eagle	GIBCO	Cat# 21010-046
DMEM/F12 with glutamax	Life Technologies	Cat# 10565-018
Penicillin/Streptomycin (10,000U/mL)	Life Technologies	Cat# 15140-122
L-Glutamine	GIBCO	Cat# 25030081
Glutamax	Life Technologies	Cat# 35050-061
Glucose	Sigma Aldrich	Cat# G8769
$NaHCO_3$	Sigma Aldrich	Cat# S5761
Transferrin	Sigma Aldrich	Cat# T3309
N2	Life Technologies	Cat# 17502-048
B27	Life Technologies	Cat# 35050-044
Doxycycline	Millipore	Cat# 324385
BDNF	Peprotech	Cat# 450-02
NT3	Peptrotech	Cat# 450-03
Laminin	ThermoFisher	Cat# 23017-015
Non-essential amino acids	Life Technologies	Cat# 11140-050

(*Continued on next page*)

Please cite this article in press as: Jang et al., Choroid plexus-CSF-targeted antioxidant therapy protects the brain from toxicity of cancer chemotherapy, Neuron (2022), https://doi.org/10.1016/j.neuron.2022.08.009

Continued

REAGENT or RESOURCE	SOURCE	IDENTIFIER
Puromycin	InvivoGen	Cat# ant-pr-1
10X HBSS	GIBCO	Cat# 14180-020
1X PBS	GIBCO	Cat# 10010023
Liberase TL	Roche	Cat# 5401020001
Accutase	Innovative Cell Tech	Cat# AT 104-500
DNAse I	Roche	Cat# 104159
Trypsin	Worthington	Cat# 3703
Calf serum	Hyclone	Cat# SH30072.03
Goat serum	Jackson	Cat# 005000121; RRID: AB_2336990
AraC, Cytosine 1-β-d-arabinofuranoside	Millipore Sigma	Cat# C1768; CAS: 147-94-4
Polybrene	Sigma	Cat# TR-1003-5
96-well plate	Grenier	Cat# 655090
Poly-ornithine	Sigma	Cat# P2533
Poly-D-lysine	Millipore Sigma	Cat# P6407; CAS: 27964-99-4
Geltrex	Life Technologies	Cat# A1413301
Cell TAK	Corning	Cat# 354240
Paraformaldehyde	Millipore Sigma	Cat# P6148; CAS: 30525-89-4
OCT compound	Fisher Healthcare	Cat# 23730571
Fluoromount-G	Fisher Scientific	Cat# OB10001
Triton X-100	Millipore Sigma	Cat# T9284; CAS: 9036-19-5
Taqman fast universal PCR master mix	Applied Biosystems	Cat# 4366072
RIPA lysis and extraction buffer	Thermo Scientific	Cat# 89900
Halt protease and phosphatase inhibitor cocktail	Thermo Scientific	Cat# 78400
NuPAGE 4-12% Bis-Tris protein gels	Invitrogen	Cat# NP0336
NuPAGE LDS sample buffer	Invitrogen	Cat# NP0007
NuPAGE sample reducing agent	Invitrogen	Cat# NP0009
GE healthcare Amersham ECL select	Fisher Scientific	Cat# 45-000-999
Amersham hybond P membranes, PVDF	Millipore Sigma	Cat# GE10600029
Metabolomics QreSS Standard 1 (labelled)	Cambridge Isotope Libraries	Item Number: MSK-QRESS1-1
Metabolomics QreSS Standard 2 (labelled)	Cambridge Isotope Libraries	Item Number: MSK-QRESS2-1
(+)- Sodium L-ascorbate	Sigma-Aldrich	CAS: 134-03-2
Metabolomics Amino Acid Mix Standard (Labeled)	Cambridge Isotope Laboratories	Item Number: MSK-A2-1.2
Glutathione (Peptide Purity 95%+) (GLYCINE-13C2, 98%+;15N, 96-99%) 90% + NET PEPTIDE CNLM-6245-HP-10	Cambridge Isotope Laboratories	CAS: #:NA, PSO #:19A-0320
Aminopterin	Shircks Laboratories	Product no. 16. 330
Ellman's reagent	Sigma-Aldrich	CAS: 69-78-03
Ammonium Carbonate (LCMS Grade)	Sigma-Aldrich	CAS: 506-87-6
Ammonium Hydroxide Solution (LCMS Grade)	Honeywell / Fluka	Cat# 44273-100ML
Acetonitrile (LCMS Grade)	Fisher Chemical	CAS: 75-05-8
Water (LCMS Grade)	Fisher Chemical	CAS: 7732-18-5
Critical commercial assays		
Methotrexate ELISA kit	Enzo Life Sciences	Cat# 142-0001
Seahorse XF cell mito stress test kit	Agilent Technologies	Cat# 103015-100
CyQUANT cell proliferation assay	Fisher Scientific	Cat# C7026
Superoxide dismutase assay kit	Cayman Chemical	Cat# 706002
TBARS assay kit	Cayman Chemical	Cat# 10009055

(*Continued on next page*)

Please cite this article in press as: Jang et al., Choroid plexus-CSF-targeted antioxidant therapy protects the brain from toxicity of cancer chemotherapy, Neuron (2022), https://doi.org/10.1016/j.neuron.2022.08.009

Continued

REAGENT or RESOURCE	SOURCE	IDENTIFIER
Glutathione peroxidase assay kit	Cayman Chemical	Cat# 703102
RNeasy micro kit	Qiagen	Cat# 74004
iScript cDNA synthesis kit	Bio-Rad	Cat# 1708891
Deposited data		
Raw metabolomics data	NIH common fund's national metabolomics data repository (NMDR)	https://www.metabolomicsworkbench.org/databases/metabolitedatabase.php
Anti-oxidative metabolism measurement in CSF of mice by quantitative LC/MS method to analyze effect of MTX on level of antioxidants in mouse controls 0-48 h in CSF and hippocampus.	NIH common fund's national metabolomics data repository (NMDR)	ST001974
Anti-oxidation metabolism measurement in mouse CSF by quantitative LC/MS method to establish MTX effects on mouse metabolism in mouse controls 0-48 h in CSF (repeat of 20200124 ChP-MTX-Anti-oxidative-study-test)	NIH common fund's national metabolomics data repository (NMDR)	ST001975
Anti-oxidative metabolism measurement in mouse CSF by quantitative LC/MS method of mouse CSF at 24 h of MTX treatment, for either control GFP or SOD3-overexpressing ChP mice.	NIH common fund's national metabolomics data repository (NMDR)	ST001976
Anti-oxidation metabolism measurement in mammalian cells and tissues by quantitative LC/MS method of human patient/lymphoma patient CSF.	NIH common fund's national metabolomics data repository (NMDR)	ST001977
Anti-oxidation metabolism measurement in human patient CSF by quantitative LC/MS method.	NIH common fund's national metabolomics data repository (NMDR)	ST001978
Anti-oxidation metabolism measurement in mouse CSF by quantitative LC/MS method.	NIH common fund's national metabolomics data repository (NMDR)	ST001979
Experimental models: Cell lines		
Primary rat cerebellar granule neurons	Lehtinen et al., 2006	N/A
Human iPSC-derived cortical neurons	Boston Children's Hospital Human Neuron Core	N/A
Experimental models: Organisms/strains		
Rat: Sprague Dawley	Charles River Laboratories	Cat# 400
Mouse: CD-1	Charles River Laboratories	Cat# 022
Mouse: CX3CR-1GFP	The Jackson Laboratory	Cat# 005582; RRID: IMSR_JAX:005582
Oligonucleotides		
Eukaryotic 18s rRNA endogenous control (VIC-MGB probe)	Thermo Fisher Scientific	Cat# 4319413E
Mouse SOD3 (FAM-MGB, Assay ID: Mm01213380_s1)	Thermo Fisher Scientific	Cat# 4453320
Human SOD1 (FAM-MGB, Assay ID: Hs00533490_m1)	Thermo Fisher Scientific	Cat# 4331182
Human SOD2 (FAM-MGB, Assay ID: Hs00167309_m1)	Thermo Fisher Scientific	Cat# 4331182
Human SOD3 (FAM-MGB, Assay ID: Hs04973910_s1)	Thermo Fisher Scientific	Cat# 4453320

(*Continued on next page*)

Please cite this article in press as: Jang et al., Choroid plexus-CSF-targeted antioxidant therapy protects the brain from toxicity of cancer chemotherapy, Neuron (2022), https://doi.org/10.1016/j.neuron.2022.08.009

Continued

REAGENT or RESOURCE	SOURCE	IDENTIFIER
Recombinant DNA		
pAAV-IRES-HrGFP	Agilent Technologies	Cat# 240075
pcDNA3.1-myc HisA (-) human SOD3	Ota et al., 2016	N/A
Software and algorithms		
ImageJ	NIH	https://imagej.nih.gov/ij/, RRID: SCR_002285
Zen	Zeiss	http://www.zeiss.com
ArrayScan XTI	ThermoFisher Scientific	http://assets.thermofisher.com
FlowJo software 10.6	BD Biosciences	http://www.bdbiosciences.com
Wave software 2.6	Agilent Technologies	http://www.agilent.com
GraphPad prism 7.04	GraphPad	https://www.graphpad.com/scientific-software/prism/; GraphPad Prism, RRID: SCR_002798
Tracefinder Peak Analysis Software	ThermoFisher	Cat# OPTON-31001
Xcalibur Software	ThermoFisher	Cat# OPTON-30965
Other		
Agilent seahorse XFe96 analyzer	Agilent Technologies	http://www.agilent.com
Pellet pestle cordless motor homogenizer	Fisher Scientific	Cat# 12-141-362
EMD Millipore ZIC-HILIC (100 x 2.1 mm, 3.5 um)	EMD Millipore	Cat# 150441
Thermo Q Exactive Orbitrap Plus (Mass Spectrometer)	ThermoFisher	Cat# IQLAAEGAAPFALGMBDK
Vanquish HPLC System	ThermoFisher	Model # VF-P10-A

RESOURCE AVAILABILITY

Lead contact

Further information and requests for resources and reagents should be directed to and will be fulfilled by the lead contact, Maria K. Lehtinen, maria.lehtinen@childrens.harvard.edu.

Materials availability

No new reagents generated.

Data and code availability

1. Data availability: Raw metabolomics data are uploaded to the NIH Common Fund's National Metabolomics Data Repository (NMDR) and are available at the Metabolomics Workbench Metabolite Database (https://www.metabolomicsworkbench.org/databases/metabolitedatabase.php). Accession numbers for the data are: 2023--1-25 - ST001979; ST001978; ST001977; ST001976; ST001975; ST001974 - Boston Children's Hospital, Harvard Medical School.
   Single-cell RNA-seq data are published (Dani et al., 2021). Microscopy data and original western blots reported in this paper will be shared by the lead contact upon request.
2. Code availability: The code used in this manuscript is available at: https://github.com/LehtinenLab/Jang2022
3. Availability of other source data and any additional information required to reanalyze the data reported in this paper are available from the lead contact upon request.

EXPERIMENTAL MODEL AND SUBJECT DETAILS

Animal studies

All animal studies were performed under the protocol approved by the Institutional Animal Care and Use Committee (IACUC) of Boston Children's Hospital. CD-1 mice (timed pregnant and 6-8 weeks, Charles River Laboratories), *Cx3cr1-GFP*$^{+/-}$ (adult mice, Jackson Laboratories), and Sprague Dawley rats (6-8 weeks, Charles River Laboratories) were purchased. Male and female animals were used in all experiments. Sex is not reported to be associated with toxicity of cancer chemotherapy and, therefore, was not specifically evaluated in these studies. All animals were housed in a 12 h light-dark cycle with *ad libitum* access to food and water.

CSF samples

Mouse CSF was collected by inserting a glass capillary into the cisterna magna and processed as described (Lehtinen et al., 2011). It was visually inspected for purity, and samples were centrifuged at 10,000 g for 10 min at 4°C prior to immediate analysis or storage at -80°C. De-identified human CSF samples from both central nervous system (CNS) lymphoma patients and non-chemotherapy-exposed controls were obtained under Beth Israel Deaconess Medical Center (BIDMC) Institutional Review Board (IRB)-approved protocols and analyzed under Boston Children's Hospital IRB-approved protocols. Samples were aliquoted and stored at -80°C until use. We were not powered to determine if sex would influence findings of this study. All samples available for this study were included in analyses as presented. Clinical information relating to diagnosis and date of sample collection is listed in Tables S1 and S2.

Human iPSC and automated imaging platform

Human iPSC-derived cortical neurons were prepared by the Human Neuron Core at BCH using a protocol from Südhof and colleagues (Zhang et al., 2013) with minor changes (Winden et al., 2019). The differentiation protocol was initiated with human iPSCs dissociated into single cells using Accutase (Innovative Cell Tech) and seeded onto Geltrex- (Life Technologies) coated plates. The iPSCs were then transduced overnight with lentiviruses expressing rtTA-, EGFP-, and NGN2 along with polybrene (Sigma). Transduced iPSCs were expanded as colonies before being dissociated to single cells by Accutase and plating on Geltrex-coated plates at a density of 5 million iPSCs per 10 cm dish to initiate the differentiation. NGN2 expression was induced on day 0 using doxycycline (2ug/mL; Millipore) and the growth factors BDNF (10ng/mL; Peprotech), NT3 (10ng/mL; Peprotech), and laminin (0.1mg/L; ThermoFisher) in N2 media for the first two days. N2 media contains DMEM/F12 with glutamax (Life Technologies), N2 (Life Technologies), and nonessential amino acids (Life Technologies). On days 1 and 2, puromycin (1ug/mL; InVivoGen) was added to select for transduced cells. On days 2-6, cells were fed with BDNF, NT3, laminin, doxycycline, and Ara-C (2uM; Sigma Aldrich) in B27 media and half media changes were performed every other day until differentiation day 6 when cells were dissociated with papain (Worthington). B27 media contains Neurobasal-A media (Life Technologies), B27 (Life Technologies), and Glutamax (Life Technologies). Following dissociation, cells were plated in neuronal growth media with BDNF, NT3 and laminin. Neuronal growth media contains Neurobasal-A media, Glutamax, Pen/Strep (Life Technologies), B27, Glucose (Sigma Aldrich), $NaHCO_3$ (Sigma Aldrich), and Transferrin (Sigma Aldrich) and was previously conditioned by an astrocyte culture to include factors that are released by astrocytes to support neuronal health. To assess ROS production, neurons were plated at a density of 20,000 neurons per well in a PDL (100ug/mL; Sigma catalog) and laminin- (5ug/mL) coated 96-well plate (Grenier), treated with vehicle or 10 μM MTX for 3 days, and then stained with CellROX Deep Red Reagent (5 μM; Life Technologies) for 30 min. Cells were imaged and analyzed using ArrayScan XTI (Thermo Fisher Scientific).

METHOD DETAILS

Methotrexate treatment paradigms

Acute paradigm: CD-1 and *Cx3cr1-GFP*$^{+/-}$ mice or Sprague Dawley rats were given a single intravenous injection of 75 mg/kg MTX (Fisher Scientific) dissolved in 0.9 % NaCl (Mountainside Medical) for 24 h or 48 h. MTX was freshly prepared for each experiment. MTX in mouse serum or CSF was assessed by MTX ELISA according to the manufacturer's instructions (Enzo Life Sciences). *Chronic paradigm*: Mice received intraperitoneal (i.p.) injections of 100 mg/kg MTX prepared as above at 3, 4, and 5 weeks of age, followed by behavioral testing at 9 weeks (Gibson et al., 2019).

Behavior analysis

Adult male and female CD-1 mice were tested in all behavior paradigms.

Grip strength

Neuromuscular function was analyzed using grip strength performance. Each trial consisted of a mouse gripping the grid with its forelimb. Once the grasp was released, maximum force was recorded (Harvard Apparatus). The average of five consecutive trials was taken as an index of forelimb grip strength.

Rotarod

Motor coordination and balance was analyzed using rotarod. The experiment consisted of two phases: training and testing phase. Training phase: To acclimate the movement of the rotarod, the mouse initially underwent a training session (IITC Life Science Inc.) during which the rod was maintained at 5 rpm for 5 min. Testing phase: On the following day, the mouse was placed on the rod as it accelerated from 5 to 40 rpm during the course of 5 min. The latency to fall from the rod was recorded automatically. The average of four trials is presented.

Open Field

For social anxiety assessment, the open field test was performed in an arena measuring 40 cm^2 in which the center area measured 20 cm^2 (Kinder Scientific). Each mouse explored the arena for 15 min. Video analysis and data acquisition were obtained with Noldus EthoVision XT video tracking software (version 15.0, Noldus Information Technologies) to analyze percent time spent in the center.

Novel object recognition test

Recognition memory was conducted in an opaque white open field arena (40 × 60 × 23 cm) and consisted of two phases, a 10 min training phase and a 5 min testing phase. During the training phase, the mouse was allowed to freely explore two identical objects for

Please cite this article in press as: Jang et al., Choroid plexus-CSF-targeted antioxidant therapy protects the brain from toxicity of cancer chemotherapy, Neuron (2022), https://doi.org/10.1016/j.neuron.2022.08.009

10 min, after which it was returned to the home cage. The open field and the objects were cleaned with Clidox to avoid odor-based bias. One clean familiar object from the training phase and one clean novel object were placed in the arena. 10 min after the end of the training phase, each mouse was returned to its open field for a 5 min testing phase. The mouse was allowed to freely explore the familiar object and the novel object. Both phases were videotaped and scored with EthoVision XT video tracking software (version 15.0, Noldus Information Technologies).

Y-maze

Spatial learning memory assessment was conducted using a symmetrical Y-maze made of clear plexiglass. Each arm of the Y-maze was 35 cm long and the wall at the end of each arm was marked with a different black and white pattern. To reduce anxiety, light in the testing room was dimmed to 30 ± 5 lux. The experiment consisted of two phases: a 10 min training phase followed by a 5 min testing phase. During the training phase, the mouse was placed at the end of the start arm, away from the center, facing the wall. The mouse was then free to explore two of the maze's arms, whereas entry into the third arm was blocked. After the training phase, the mouse was returned to its home cage for a 30 min inter-trial interval. During the testing phase, the block in the third arm was removed, the mouse was placed back in the start arm, and the mouse was then allowed to access all three arms of the maze. The maze was cleaned with Clidox to avoid odor-based bias after each session. Video analysis and data acquisition were obtained with Noldus Etho-Vision XT video tracking software (version 15.0, Noldus Information Technologies) to analyze percent time spent in the novel (third) arm.

Elevated plus maze (EPM)

Anxiety behavior was analyzed using EPM. The EPM apparatus consisted of two open arms (35.5 × 6 cm) and two closed arms (35.5 × 6 cm) radiating from a central area (6 × 6 cm) (Med Associates Inc.). At the start of a trial, the mouse was placed in the center and allowed to explore the maze for 5 min. Infrared light illuminated the arms and the total time spent in each arm was tracked and scored using Noldus Etho-Vision XT video tracking software (version 15.0, Noldus Information Technologies). The apparatus was cleaned with Clidox to avoid odor-based bias before and after each session. The testing room was dimly lit with luminosity of approximately 30 lux.

AAVs

The pAAV-IRES-hrGFP vector was purchased (Agilent Technologies) and pcDNA3.1-myc HisA (-) / human SOD3 (myc-his tag at C-terminal) was share by Ota et al. (2016). Virus production and purification were performed by the Viral Core at BCH according to standard procedures (Grieger et al., 2006).

In utero i.c.v. injections

Timed pregnant CD-1 mice (E13.5) were anesthetized with isoflurane inhalation, and laparotomy was performed. AAV5-CMV-hrGFP or AAV5-CMV-hSOD3 was delivered into lateral ventricles using fine glass capillary pipettes (Drummond Scientific Company) as in Kaiser et al. (2021) and Xu et al. (2021). Meloxicam analgesia was used following surgery.

mRNA expression analyses

Total RNA was isolated using RNeasy Micro Kit (Qiagen, 74004) and reverse transcribed with iScript™ cDNA synthesis (Bio-Rad, 1708891) according to the manufacturer's instructions. Taqman gene expression probes (Thermo Fisher Scientific) were used for qRT-PCR performed on a StepOne Plus (Applied Biosystems) instrument. 18S rRNA served as internal control.

Immunohistochemistry

Animals were perfused with phosphate-buffered vehicle (PBS) followed by 4% paraformaldehyde (PFA), dissected, and post-fixed with 4% PFA overnight. Following cryoprotection, samples were frozen in OCT and cryosectioned at 14 μm thickness. Sections were incubated with blocking buffer (5% goat serum/0.3% triton X-100 in PBS) for at least 1 h at room temperature and then incubated with primary antibodies in blocking buffer overnight at 4°C (for sections: chicken anti-GFP 1:1000; rat anti-CD68 1:200). Following PBS washes, sections were incubated with fluorescent secondary antibodies (1:1000; Thermo Fisher Scientific) in blocking buffer for 2 h at room temperature. Following PBS washes, sections were incubated with Hoechst (1:5000 in PBS) for 10 min before final wash with PBS. Sections were mounted with Fluoromount-G.

Macrophage quantification in brain sections

Images were obtained with a 20X objective using a Zeiss LSM 880 with Fast Airyscan. Images were analyzed using ImageJ. The ChP was outlined by hand to determine the perimeter of the structure. Macrophages present on the apical side of the ChP, distinguished from those in the stromal space by their anatomical position relative to the nuclear staining of the ChP, were counted in each section. The "density" of intraventricular macrophages was determined by dividing the number of apical macrophages present on the ChP or in the ventricle by the perimeter of the ChP in mm. Three images on three separate sections were used and averaged per animal.

ChP whole mount preparation

Following perfusion, the ChP explants were dissected and post-fixed in 4% PFA for an additional 12-15 min. No additional immunostaining was performed on AAV-transduced ChP for GFP expression. Hoechst (1:5000 in PBS) was applied for 15 min. Explants were washed with PBS prior to mounting flat on slides.

Immunoblotting

Tissues were homogenized using RIPA Lysis and Extraction Buffer (Thermo Scientific) containing Halt Protease and Phosphatase Inhibitor Cocktail (Thermo Scientific). Equal amounts of protein were loaded and separated by SDS-polyacrylamide gel electrophoresis (SDS-PAGE) on NuPage gels (Invitrogen) and transferred to polyvinylidene difluoride membrane (PVDF, Millipore). Membranes were probed with primary antibodies and detected by horseradish peroxidase (HRP)-conjugated secondary antibodies and ECL Detection Reagent (GE Healthcare).

Ex vivo ChP culture and MTX treatment

Lateral ventricle (LV) and fourth ventricle (4V) ChP were dissected and incubated with or without 10 μM MTX in neurobasal medium (GIBCO) supplemented with penicillin-streptomycin (100 U/mL penicillin and 100 μg/mL streptomycin; GIBCO) and glutamine (2 mM). A dose-response curve (1 nM - 50 μM MTX) with human neurons indicated sensitivity at 10 μM MTX (compared with DMSO control), matching a prior report (Seigers et al., 2008). Fluorescent MTX (2 μM) was also applied to ChP explants (Breen et al., 2004) (Thermo Fisher Scientific).

Flow cytometry analysis

LV and 4V ChP explants were enzymatically digested to create a single cell suspension with Liberase TL (100 μg/ml; Roche) for 30 min at 37°C. Samples were then triturated and passed through a 100 μm filter. After centrifugation at 2,000 rpm for 5 min at 4°C, dissociated cells were washed twice in ice cold FACS buffer (PBS containing 1% BSA and 2 mM EDTA). To compare the membrane potential between vehicle- or 10 μM MTX-treated ChP, samples were incubated with MitoTracker Deep Red (500 nM; Thermo Fisher Scientific) for 20 min. To assess ROS production between vehicle- or 10 μM MTX-treated ChP, samples were stained with CellROX Deep Red Reagent (5 μM; Life Technologies) for 30 min. Cells were then washed and resuspended in FACS buffer followed by immediate analysis via flow cytometery-based FACSVerse (BD Biosciences). Data were analyzed using FlowJo software 10.6 (BD Biosciences).

Rat cerebellar granule cell cultures and survival assay

Cerebellar granule neurons were prepared from postnatal 6 (P6) rat pups as described (Lehtinen et al., 2006). Briefly, after 3 days of culture *in vitro*, culture medium was changed to contain 20% artificial CSF or 20% native, adult rat CSF (Lehtinen et al., 2011). Cells were then treated with vehicle or 100 μM H_2O_2 for 24 h, fixed, counterstained with Hoechst 33342 (Thermo Scientific), and scored for survival based on nuclear health as described (Lehtinen et al., 2006). Cell counts were carried out in a blinded manner, and a minimum of 150 cells were counted per experiment.

Seahorse metabolic analysis

For mitochondrial function assays, 10,000 human iPSC-derived cortical neurons or the posterior leaflet of LV ChP were/was plated in poly-D-lysine-coated (Sigma-Aldrich) or Cell TAK (Corning)-coated Seahorse assay spheroid wells (Agilent Technologies), respectively. Following treatment with vehicle or 10 μM of MTX for 2 h at 37°C, oxygen consumption rate (OCR) was measured with the Cell Mito Stress Test (Agilent Technologies) with an Agilent Seahorse XFe96 Analyzer (Agilent Technologies) according to the manufacturer's instructions. Data were analyzed using Wave software (Agilent Technologies). Data were normalized to DNA content on a per well basis, determined by CyQUANT Cell Proliferation Assay (Invitrogen). OCR was used to calculate different domains of mitochondrial function metrics by sequentially applying oligomycin (ATP synthase inhibitor), FCCP (collapses the proton gradient and disrupts the mitochondrial membrane potential) and a mix of antimycin A (complex III inhibitor) and rotenone (complex I inhibitor).

Biochemical assays

Relative SOD activity was measured in mouse or rat CSF samples using the Superoxide Dismutase Assay Kit (Cayman Chemical) according to the manufacturer's instructions. TBARS Assay (Cayman Chemical) and Glutathione Peroxidase Assay (Cayman Chemical) kits were used to measure oxidative stress according to the manufacturer's instructions.

LC-MS-based metabolite profiling

For characterization by mass spectrometry, mouse CSF was acquired 4 h, 24 h, and 48 h following a single 75 mg/kg MTX injection from 6-8 mice and flash frozen for further analysis. Per condition, 3 μL of CSF was extracted by brief sonication in 240 μL 100% methanol, supplemented with isotopically labeled internal standards (17 amino acids and reduced glutathione, Cambridge Isotope Laboratories, MSK-A2-1.2 and CNLM-6245-10) and 60 μL 20 mM Ellman's reagent in water (Sigma-Aldrich, D8130). After centrifugation for 10 min at maximum speed in a benchtop centrifuge (Eppendorf), the cleared supernatant was dried using a nitrogen dryer and reconstituted in 30 μL water by brief sonication. Extracted metabolites were spun again, and cleared supernatant was transferred to LC-MS microvials. A small amount of each sample was pooled and serially diluted 3- and 10-fold to be used as quality controls throughout the run of each batch. Two microliters (equivalent to 0.2 μL of CSF) of reconstituted sample were injected into a ZIC-pHILIC 150 × 2.1 mm (5 μm particle size) column (EMD Millipore) operated on a Dionex UltiMate 3000 UPLC system (Thermo Fisher Scientific). Chromatographic separation was achieved using the following conditions: buffer A was acetonitrile; buffer B was 20 mM ammonium carbonate, 0.1% ammonium hydroxide. Gradient conditions were: linear gradient from 20% to 80% B; 20–20.5 min: from

80% to 20% B; 20.5–28 min: hold at 20% B. The column oven and autosampler tray were held at 25°C and 4°C, respectively. MS data acquisition was performed by a QExactive benchtop Orbitrap mass spectrometer equipped with an Ion Max source and a HESI II probe and was performed in a range of m/z = 70–1,000, with the resolution set at 70,000, the AGC target at $1x10^6$, and the maximum injection time (Max IT) at 20 msec. For tSIM scans, the resolution was set at 70,000, the AGC target was $1x10^5$, and the max IT was 100 msec. Relative quantitation of polar metabolites was performed with TraceFinder 4.1 (Thermo Fisher Scientific) using a 5 ppm mass tolerance and referencing an in-house library of chemical standards. Pooled samples and fractional dilutions were prepared as quality controls. Metabolites were taken for further analysis only if the correlation between the dilution factor and the peak area was >0.95 (high confidence metabolites). Normalization for biological material amounts was based on the total integrated peak area values of high-confidence metabolites within an experimental batch after normalizing to the averaged factor from all mean-centered chromatographic peak areas of isotopically labeled amino acid internal standards (Cambridge Isotope Laboratories). The data were log transformed and Pareto scaled for MetaboAnalyst-based statistical or pathway analysis (Xia et al., 2015). We profiled 200 metabolites, 85 of which were detected in CSF and passed our quality control protocol.

Single cell transcriptomics

Mouse embryonic ChP single cell RNA-seq dataset was acquired and analyzed in Dani et al. (2021). Briefly, whole embryonic ChP tissue from each ventricle was micro-dissected and digested, and live cells were FACS sorted. Single cells (~7,000 cells) were processed through the 10X Genomics Single Cell 3' platform.

Variable genes were selected by using the method described in Montoro et al. (2018). Briefly, a logistic regression model was fit to the cellular detection fraction as a function of total numbers of unique molecular identifiers (UMIs) per cell. Outliers from this curve (i.e., genes expressed in fewer cells than expected given the number of UMIs) were genes that contained more variance than proportionally expected, and, therefore, were particularly suited for reducing the dimensionality of the dataset. We used a threshold deviance of -0.15 and determined the variable genes independently for each of three experimental replicates. The genes that were at the intersection of these three replicate gene lists (i.e., global variable genes) were used for downstream analysis. The expression matrix was restricted to the subset of these global variable genes, and then centered and scaled before performing principal component analysis (PCA) using *Seurat*'s RunPCA() function. After PCA, the number of significant principal components was determined to be 5 using the elbow method. The data were then visualized as a 2D embedding of the significant principal components using t-SNE (Kobak and Berens, 2019) via the RunTSNE() function in *Seurat*.

Statistics

All statistical analyses were performed with GraphPad Prism 9.2 (GraphPad Software). Most analyses were performed using one-way ANOVA with multiple comparison (Tukey) or student's two-tailed unpaired t-test. All statistical analyses used, including exact values of n and what n represents are indicated in the corresponding figure legends. Data are presented as mean ± S.E.M., and p values < 0.05 were considered significant (*$p < 0.05$, **$p < 0.01$, ***$p < 0.001$, ****$p < 0.0001$).